

Short-Term Space Occupancy and Conjunction Filter

Ana S. Rivero *

University of Seville, 41092 Seville, Spain

Claudio Bombardelli[†]

Technical University of Madrid (UPM), 28040 Madrid, Spain

Rafael Vazquez[‡]

University of Seville, 41092 Seville, Spain

Conjunction analysis for resident space objects (RSOs) requires estimating the range of altitudes that each object can cross, i.e. its space occupancy, throughout a screening time of, typically, a few days. The work proposes an analytical method to evaluate the space occupancy of an RSO for a time horizon of generic duration in a zonal problem model. The method, which allows one to compute the maximum and minimum occupied orbit radii by solving a quartic equation, is employed as a basis for the implementation of a new conjunction filter with a considerable performance improvement compared to the classical apogee-perigee filter. The effectiveness of the newly proposed filter is assessed in a low-Earth orbit scenario using a high-fidelity perturbation model and for a wide range of orbits and conjunction geometries. Finally, the space occupancy evaluation method is employed as a quick and effective tool to assess the degree of radial overlap of RSOs in low-earth orbit and its evolution in the last decade.

Nomenclature

a	=	dimensionless osculating semimajor axis
a_{sp}	=	short-periodic term of semimajor axis
\hat{a}	=	dimensionless mean semimajor axis
B	=	ballistic coefficient, $\text{m}^2 \cdot \text{kg}^{-1}$
B^*	=	drag term, $\text{m}^2 \cdot \text{kg}^{-1}$
b_{AP}	=	AP-filter model error buffer, km
b_{SO}	=	SO-filter model error buffer, km
E	=	eccentric anomaly, rad
e	=	osculating eccentricity

*Ph.D. Candidate, Aerospace Engineering Department, asanchez8@us.es.

[†]Associate Professor, Space Dynamics Group, claudio.bombardelli@gmail.com

[‡]Professor, Aerospace Engineering Department, rvazquez1@us.es.

e_f	=	Cook's frozen eccentricity
e_p	=	proper eccentricity
e_{sp}	=	short-periodic term of eccentricity
\hat{e}	=	mean eccentricity
\hat{e}_0	=	initial mean eccentricity
h	=	altitude variation due to atmospheric drag, km
h_0	=	initial altitude, km
i	=	osculating inclination, rad
i_{sp}	=	short-periodic term of inclination, rad
\hat{i}	=	mean inclination, rad
J_2	=	oblateness coefficient
J_3	=	third spherical harmonic coefficient
k	=	frequency of Cook's eccentricity vector
M	=	osculating mean anomaly, rad
M_{sp}	=	short-periodic term of mean anomaly, rad
\hat{M}	=	"mean" mean anomaly, rad
P_n^1	=	Legendre function of order one and degree n
R_{\oplus}	=	Earth radius, km
r	=	orbital radius
r_N	=	minimum radial distance of frozen orbit
r_S	=	maximum radial distance of frozen orbit
r_f	=	frozen orbit radius
r_{max}	=	maximum radius over a fix time interval
$r_{max,L}$	=	maximum radial distance of a generic, non-frozen orbit
$r_{max,i}$	=	i-orbit maximum radius, km
r_{min}	=	minimum radius over a fix time interval
$r_{min,L}$	=	minimum radial distance of a generic, non-frozen orbit
$r_{min,i}$	=	i-orbit minimum radius, km
$\hat{r}_{p0,i}$	=	i-orbit mean perigee radius at the reference time, km
$\hat{r}_{a0,i}$	=	i-orbit mean apogee radius at the reference time, km
SOR	=	space occupancy range
α	=	initial angular condition of Cook's eccentricity vector, rad

β	=	rotation angle of Cook's circle, rad
β_a	=	constant of the exponential model fit of the atmospheric density, km^{-1}
(ξ, η)	=	mean eccentricity vector perifocal components
θ	=	argument of latitude, rad
$\hat{\theta}$	=	mean argument of latitude, rad
ν	=	true anomaly, rad
ρ	=	atmospheric density, $\text{kg}\cdot\text{m}^{-3}$
$\bar{\rho}$	=	constant of the exponential model fit of the atmospheric density, $\text{kg}\cdot\text{m}^{-3}$
τ	=	dimensionless time
Ω	=	osculating right ascension of the ascending node, rad
Ω_{sp}	=	short-periodic term of right ascension of the ascending node, rad
$\hat{\Omega}$	=	mean right ascension of the ascending node, rad
ω	=	osculating argument of periapsis, rad
ω_{sp}	=	short-periodic term of argument of periapsis, rad
$\hat{\omega}$	=	mean argument of periapsis, rad
$\hat{\omega}_0$	=	initial mean argument of periapsis, rad

I. Introduction

THE space environment is becoming ever more crowded, both because of the deployment of large constellations of small to medium-sized satellites by several companies, as well as the growing number of space debris. Over the next decade, more than 20 000 satellites are projected to be placed in orbit, as proposed by approximately two dozen companies. Providing perspective for the magnitude of this number, it is worth noting that since the inception of the space age, fewer than 8 100 payloads have been launched into Earth orbit [1]. In addition, one must consider the presence of space debris in near-Earth space. The quantity of small orbital debris is increasing progressively and exceeds the number of large, cataloged space objects by several orders of magnitude [2]. Consequently, the risk of losing a satellite during a collision is increasing and not negligible [3] and if such an event were to occur, it would not only destroy the two objects involved but also generate a significant amount of debris, which can in turn produce more collisions. The impact between an Iridium satellite and COSMOS 2251 which took place in 2009 is a clear example of these circumstances [4]. To mitigate the risk of collisions, the initial step involves detecting close encounters between satellites of interest and other objects. A close encounter, or critical conjunction, occurs when the expected orbits of two satellites result in a minimum approach distance below a few kilometers (typically 5 to 10 km). Once a critical conjunction is identified, the threat level is assessed by computing the probability of collision. Finally, if this probability

is above a given threshold, a collision avoidance maneuver is carried out [5].

Considering the substantial number of Resident Space Objects (RSOs), this process is highly demanding from the computational time point of view. The problem of “all on all” conjunction screening is not usually addressed operationally due to the computational difficulties involved; the problem of comparing an entire catalog of more than 20 000 objects against itself results in more than 200 million pairs to be screened. In fact, this problem will become even more daunting in the future space environment due to the rise of space traffic and enhanced observation capabilities, which will significantly boost the number of cataloged objects and, as a result, increase the number of potential conjunction pairs [6]. Nevertheless, previous studies have attempted to find effective solutions to reduce the computational load of this problem by employing different techniques, such as filtering process or parallel computation [7–10]. Indeed, the filtering process to remove RSO pairs that practically have no chance of collision is one of the most widespread computational acceleration techniques for conjunction analyses [11]. For instance, if the object of interest is in a low Earth orbit (LEO) then objects that never enter the LEO region, as GEO objects, are discarded. Different types of filters have been proposed in the literature; the main types of filters are apogee-perigee, orbit path, and time filter. The first two are based on the geometry of the orbit [12]. The apogee-perigee filter is used to eliminate satellite pairs whose altitude band does not overlap, so they can never collide. The orbit path filter is used to rule out pairings whose distance between orbits is always greater than the keep-out threshold. The time filter is instead based on temporal coincidence among orbits that are close. The fact that two orbits are within a threshold distance of each other does not mean that a conjunction will necessarily occur; the two satellites need to be at that specified distance at the same time [13].

The apogee-perigee filter is the simplest of the three filters defined above. This filter only accepts object pairs with possibly overlapping Earth central radii (considering that the radius can vary only between its minimum and maximum, computed by finding the radius of perigee and apogee, respectively); this computation only needs to be performed once for each object, not for each pair. This is relevant for the case of “all on all” conjunction analysis, since the computational load increases by order N instead of N^2 , as it does with the other filters. However, despite its simplicity, it suffers from a major drawback: the filter is based on a Keplerian model which does not take into account the effect of perturbations. As a consequence, the inclusion of a buffer distance is needed to take into account orbit radius fluctuation induced mainly by the action of gravitational harmonics. The added buffer needs to be established in a heuristic manner, which is a delicate operation [14]. Too small a buffer poses the risk of real conjunctions to be filtered. Conversely, if the buffer is too wide, a large number of non-critical conjunctions are left unfiltered. These are the two types of errors to which filters are vulnerable; false positives, which occur when the filter determines the pair should be assessed further but a conjunction is not possible and false negatives, which happen when the filter discards the pair for further analysis but a conjunction could exist.

There are several previous works to improve the classical apogee-perigee filter. For instance, Filter I proposed by Casanova [15] deals with two of the problems of Hoot’s apogee-perigee filter [12]. First, the apogee and perigee of

each pair are computed employing the osculating elements, which are subject to perturbations, over short and long periods. The second problem is that the comparison of the perigee and apogee of two objects at some fixed time might lead to a false positive if either one is an active satellite performing a maneuver. They employ an ephemerides table to obtain the equinoctial orbital elements and obtain these elements at a generic time by linear interpolation. The main idea of this filter is to replace the computation of the perigee and apogee with the calculation of the absolute minimum and maximum of the geocentric distance at a precise instant of time. Two other methods for improving this filter are proposed by Woodburn [10]. The first method involves adding a padding to the detection threshold and sampling each trajectory at the beginning and the end of the analysis interval to determine the range of radial distances for each object. The reason for sampling at both ends of the analysis interval is to capture the effects of trends in the apogee or perigee. The other method follows the same idea as Filter I, to sparingly sample all trajectories to determine the minimum and maximum radial distance for each one, but this method requires more computational load.

A recent work by Bombardelli et al. [16] introduced the concept of space occupancy as a mean to organize the distribution of RSOs in non-overlapping orbital shells thereby reducing the number of required collision avoidance maneuvers. Because the focus of that work was to provide possible solutions for an optimized RSOs distribution in the long term (a few months or longer), space occupancy was considered for a time scale long enough to allow a full rotation of the line of apsides for the great majority of LEO objects. This "long-term space occupancy" was shown to be strongly related to the geometry of frozen orbits and the concept of proper eccentricity pioneered by Cook in 1966 [17]. For conjunction screening purposes, which are performed with a time horizon significantly shorter than the line of apsides precession period, the analytical relations derived in [16] are too conservative in most cases and need to be generalized accounting for an arbitrarily short time interval. Such generalization is the primary objective of the present work which aims at providing a methodology to accurately and rapidly estimate the range of altitudes within which a satellite operates during a specific time interval. Moreover, this methodology is employed as the basis for the design of a new conjunction filter improving the performance of the classical apogee-perigee filter by accurately modeling the effect of zonal harmonics on the range of motion of an RSO. The newly designed filter, denoted as space occupancy conjunction filter (SO-filter), is based on a zonal-perturbed two-body-problem model and can be effectively employed as an alternative to the classical apogee-perigee filter. As a second application, space occupancy tools can be used to analyze the management of space; to this end, a brief study of the space population over the years is presented at the end of this work.

The structure of the article is as follows. First, Section II revisits the space occupancy theory and introduces the concept of short-term space occupancy, whose results are validated with a high-fidelity propagator. Next, in Section III, after providing a definition and analytical implementation of several filters based on short-term space occupancy, their performance is compared with the classical apogee-perigee filter in terms of reliability and effectiveness. Finally, a brief analysis of the evolution of the space population from 2005 to the present is provided in Section IV using the developed

space occupancy tools and some final remarks are given in Section V.

II. Space Occupancy Theory

A. Long-term Space Occupancy

The concept of space occupancy was introduced in Bombardelli et al. [16] as the domain occupied by an individual satellite as it moves along its nominal orbit under the effects of environmental perturbations during a given interval of time. Space occupancy is a similar concept to the reachability domain where environmental perturbations instead of thrust acceleration are determining the boundaries of the region of space that an RSO can reach. When such interval is large enough, i.e. of the order of the J_2 -induced line of apsides precession period or longer, space occupancy has been shown to be related to the geometry of frozen orbits and the concept of proper eccentricity [16]. The main results of [16] are summarized in the following for convenience.

Consider the Earth radius R_\oplus as reference length unit and the inverse mean motion of a circular orbit of that radius as reference time unit. Denote with \hat{e} , $\hat{\omega}$, \hat{a} , and \hat{i} the mean value, i.e., averaged over the mean anomaly, of the eccentricity, argument of periapsis, semimajor axis, and inclination [18].

From the work of Cook [17], the mean eccentricity vector perifocal components:

$$\xi(\tau) = \hat{e}(\tau) \cos \hat{\omega}(\tau), \quad \eta(\tau) = \hat{e}(\tau) \sin \hat{\omega}(\tau) \quad (1)$$

obey, for small eccentricity (see also Bombardelli et al. [16]):

$$\xi(\tau) = e_p \cos \beta \quad (2)$$

$$\eta(\tau) = e_p \sin \beta + e_f \quad (3)$$

where

$$k = \frac{3J_2}{\hat{a}^{7/2}} \left(1 - \frac{5}{4} \sin^2 \hat{i} \right) \quad (4)$$

and where e_f , e_p and β are, respectively the frozen eccentricity, the proper eccentricity and the rotation angle as depicted in Fig. 1 and whose analytical expressions are ([16, 17]):

$$e_f = k^{-1} \hat{a}^{-3/2} \sum_{n=1}^N \frac{J_{2n+1}}{\hat{a}_0^{2n+1}} \frac{n}{(2n+1)(n+1)} P_{2n+1}^1(0) P_{2n+1}^1(\cos \hat{i}), \quad (5)$$

with P_n^1 indicating the associated Legendre function of order one and degree n .

$$e_p = \sqrt{(\hat{e}_0 \sin \hat{\omega}_0 - e_f)^2 + \hat{e}_0^2 \cos^2 \hat{\omega}_0} \quad (6)$$

$$\sin \alpha = \frac{\hat{e}_0 \sin \hat{\omega}_0 - e_f}{e_p}, \quad \cos \alpha = \frac{\hat{e}_0 \cos \hat{\omega}_0}{e_p}, \quad \beta = k\tau + \alpha \quad (7)$$

In the preceding expressions \hat{e}_0 and $\hat{\omega}_0$ refer to the initial mean eccentricity and argument of periapsis, i.e., at the instant $\tau = 0$.

From the above expressions, the mean eccentricity and argument of periapsis can be readily computed as:

$$\hat{e}(\tau) = \sqrt{e_f^2 + e_p^2 + 2e_f e_p \sin \beta} \quad (8)$$

$$\hat{\omega} = \tan^{-1} \left(\frac{\eta}{\xi} \right) \quad (9)$$

As outlined in [16], given a (constant) mean semimajor axis \hat{a} and inclination \hat{i} one can obtain the polar equation for the corresponding frozen orbit as a function of the mean argument of latitude $\hat{\theta}$:

$$r_f(\hat{\theta}) = \hat{a} (1 - e_f \sin \hat{\theta}) + \frac{J_2}{4\hat{a}} [(9 + \cos 2\hat{\theta}) \sin^2 \hat{i} - 6] \quad (10)$$

whose minimum and maximum radii are, respectively:

$$r_N \simeq \hat{a} (1 - e_f) + \frac{J_2 (4 \sin^2 \hat{i} - 3)}{2\hat{a}} \quad (11)$$

$$r_S \simeq \hat{a} (1 + e_f) + \frac{J_2 (4 \sin^2 \hat{i} - 3)}{2\hat{a}} \quad (12)$$

Note that the minimum radius is generally reached at “North” for the Earth case and the maximum radius is reached at “South”. However, these extremes interchange their location in those few cases where the frozen eccentricity is negative. These negative values of the e_f are achieved only in orbits with an inclination close to the critical inclination.

The frozen orbit can be used as a backbone to compute the long-term radial bounds of a generic, non-frozen orbit of equal mean semi-major axis and inclination as [16] (see also Fig. 2):

$$r_{min,L} = r_N - \frac{SOR}{2} = r_N - \hat{a}e_p \quad (13)$$

$$r_{max,L} = r_S + \frac{SOR}{2} = r_S + \hat{a}e_p \quad (14)$$

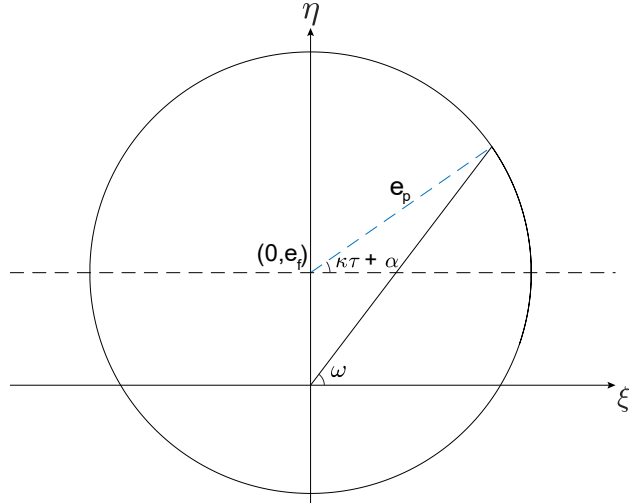


Fig. 1 Motion of the eccentricity vector in the (ξ, η) plane.

where the *space occupancy radius* (SOR) which corresponds to the maximum “mean” apoapsis minus the minimum “mean” periapsis [16]:

$$SOR \simeq \hat{a}(\hat{e}_{max} - \hat{e}_{min}) = 2\hat{a}e_p \quad (15)$$

Note that these results valid for orbits of small eccentricities, can be extended to the generic eccentricity case as far as the computation of an orbit space occupancy is concerned [16].

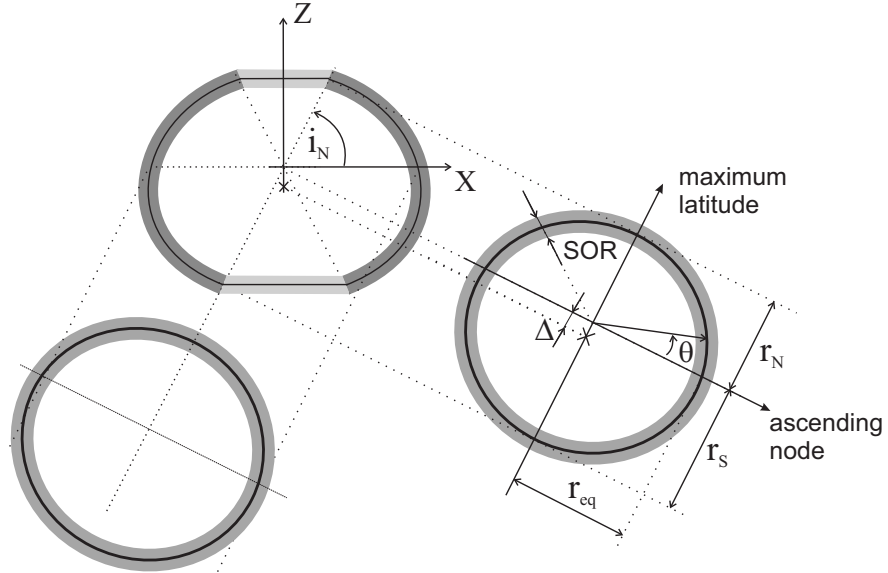


Fig. 2 Space Occupancy Geometry, credits [16].

To illustrate these bounds, Fig. 3 shows the comparison of computed apogee and perigee and $r_{max,L}$ and $r_{min,L}$ radii

values for a LEO orbit. The variation of the radius itself is also shown, as well as the changing osculating perigee and apogee.

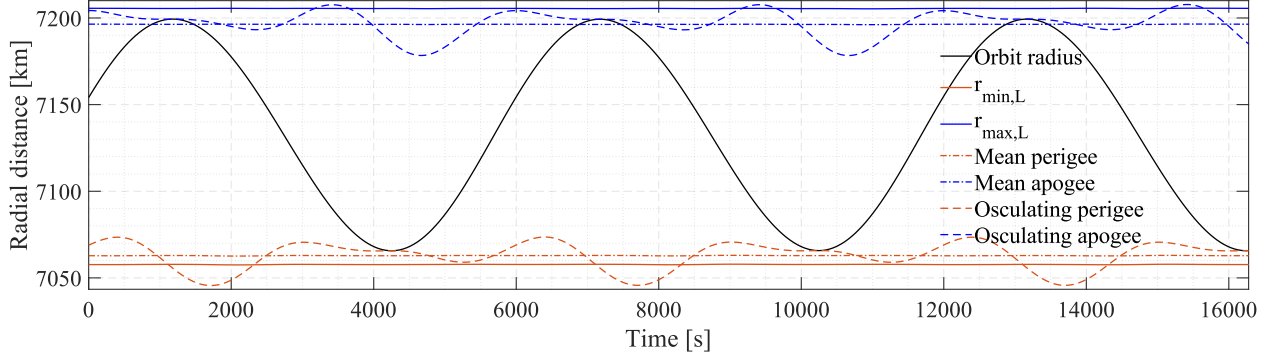


Fig. 3 Apogee, perigee, r_S and r_N for an example LEO orbit.

B. Short-term Space Occupancy Estimation

When the time interval taken for the evaluation of the space occupancy is much shorter than the line of apsides precession period, the bounds provided by Eq. (13) and (14) may be too conservative, which motivates a generalization of the space occupancy equations for an arbitrary timespan.

Instead of using the frozen orbit polar equation $r = r_f(\theta)$ with an added radius fluctuation driven by the proper eccentricity one can consider a time parameterization of the radius function $r = r(\tau)$ and estimate its lower and upper bounds across a given interval by simply imposing zero time derivative. The procedure is described in the following.

1. Time-dependent Radius Function

The radius variation of a generic non-frozen orbit can be obtained from Bombardelli et al. [16] (Eq.(12-14) of that reference) as:

$$\hat{r} \approx \hat{a} (1 - \hat{e} \cos(\hat{\theta} - \hat{\omega})) + \frac{J_2}{4\hat{a}} [(9 + \cos(2\hat{\theta})) \sin^2 \hat{i} - 6]. \quad (16)$$

All local maxima and minima of the preceding equation can be obtained by imposing:

$$\frac{dr(\tau)}{d\tau} = \frac{\partial r}{\partial \hat{e}} \frac{d\hat{e}}{d\tau} + \frac{\partial r}{\partial \hat{\omega}} \frac{d\hat{\omega}}{d\tau} + \frac{\partial r}{\partial \hat{M}} \frac{d\hat{M}}{d\tau} = 0$$

leading to:

$$-\hat{a} \frac{d\hat{e}}{d\tau} \cos \hat{M} + \hat{a} \hat{e} \sin \hat{M} \frac{d\hat{M}}{d\tau} - \frac{J_2 \sin^2 \hat{i}}{2\hat{a}} \sin(2\hat{M} + 2\hat{\omega}) \left(\frac{d\hat{M}}{d\tau} + \frac{d\hat{\omega}}{d\tau} \right) = 0 \quad (17)$$

In the preceding equation, the time derivatives of the mean eccentricity and argument of periapsis can be obtained

from Cook's relations, by deriving Eqs. (2)–(3) and (8)–(9), as:

$$\frac{d\hat{\omega}}{d\tau} \simeq \frac{1}{\hat{e}^2} \left(\frac{d\eta}{d\tau} \xi - \eta \frac{d\xi}{d\tau} \right) \quad (18)$$

$$\frac{d\xi}{d\tau} = -e_p k \sin \beta \quad (19)$$

$$\frac{d\eta}{d\tau} = e_p k \cos \beta \quad (20)$$

$$\frac{d\hat{e}}{d\tau} \simeq \frac{1}{2\hat{e}} \left(2\xi \frac{d\xi}{d\tau} + 2\eta \frac{d\eta}{d\tau} \right) \quad (21)$$

while the time derivative of the mean mean anomaly can be written, retaining only the secular part and neglecting the long-periodic contribution, as [19]:

$$\frac{d\hat{M}}{d\tau} \simeq \sqrt{\frac{1}{\hat{a}^3}} + \frac{3J_2}{2\hat{a}^2(1-\hat{e}^2)^{3/2}} \left(1 - \frac{3}{2} \sin^2 \hat{i} \right) \quad (22)$$

The computation of the global maximum and minimum of $r(\tau)$ through the numerical solution of Eq. 17 yields a very accurate although computationally expensive solution for the short-time space occupancy problem.

2. Space Occupancy Quartic Equation

Revisiting the equation found for the mean radius in terms of the argument of latitude, Eq.(16), using $\cos(\hat{\theta} - \hat{\omega}) = \cos \hat{\theta} \cos \hat{\omega} + \sin \hat{\theta} \sin \hat{\omega}$ and the definition of the eccentricity vector given in Eq. (1), the first term of Eq. (16) can be written in terms of the eccentricity vector as

$$\hat{a} (1 - \hat{e} \cos(\theta - \hat{\omega})) = \hat{a} (1 - (\xi \cos \theta + \eta \sin \theta)) \quad (23)$$

Now, using Eq. (2)–(3) in Eq. (23), one reaches

$$\begin{aligned} \hat{a} (1 - \hat{e} \cos(\theta - \hat{\omega})) &= \hat{a} (1 - e_p (\cos \beta \cos \theta + \sin \beta \sin \theta) - e_f \sin \theta) \\ &= \hat{a} (1 - e_p \cos(\theta - \beta) - \hat{a} e_f \sin \theta) \end{aligned} \quad (24)$$

which inserted into Eq. (16) leads to an equation for \hat{r} in terms of $\hat{\theta}$ and β :

$$\hat{r} \approx \hat{a} (1 - e_p \cos(\hat{\theta} - \beta) - e_f \sin \hat{\theta}) + \frac{J_2}{4\hat{a}} [(9 + \cos(2\hat{\theta})) \sin^2 \hat{i} - 6]. \quad (25)$$

In Eq. (25), the variable $\beta = k\tau + \alpha$ moves on a long time-scale, whereas the argument of latitude depends on the variation of both the true anomaly and the argument of perigee. Now, considering that the true anomaly moves much faster than β (and therefore much faster than $\hat{\omega}$), this also implies that $\hat{\theta}$ moves much faster than β . Indeed, it can be

considered that, for all effects of the short-term occupancy, $\hat{\theta}$ runs through $[0, 2\pi)$ whereas β only covers a short arc. This difference in time scales supports the assumption that the two variables β and $\hat{\theta}$ are independent, so one can write $\hat{r}(\theta, \beta)$. This allows to go from the time-domain extreme seeking of Section II.B.1 to a multivariable (but simpler) search for extreme values.

Being a continuous and differentiable function of two variables, it is a fact of calculus that its extrema lie either at critical points or at the boundary of the domain under consideration.

Assume at first that both $\hat{\theta}$ and β can move through all possible values. Since \hat{r} is a periodic function, and the domains of $\hat{\theta}$ and β are compact and have no boundaries, basic results of calculus imply that there is a global maximum and minimum which is necessarily located at a critical point (or else the function is a constant).

To locate the critical points, the first step is finding both the first and second derivatives of \hat{r} with respect to $\hat{\theta}$ and β :

$$\frac{\partial \hat{r}}{\partial \beta} = -\hat{a}e_p \sin(\hat{\theta} - \beta), \quad (26)$$

$$\frac{\partial \hat{r}}{\partial \hat{\theta}} = \hat{a} (e_p \sin(\hat{\theta} - \beta) - e_f \cos \hat{\theta}) - \frac{J_2 \sin^2 \hat{i}}{2\hat{a}} \sin(2\hat{\theta}), \quad (27)$$

$$\frac{\partial^2 \hat{r}}{\partial \beta^2} = \hat{a}e_p \cos(\hat{\theta} - \beta), \quad (28)$$

$$\frac{\partial^2 \hat{r}}{\partial \beta \partial \hat{\theta}} = -\hat{a}e_p \cos(\hat{\theta} - \beta), \quad (29)$$

$$\frac{\partial^2 \hat{r}}{\partial \hat{\theta}^2} = \hat{a} (e_p \cos(\hat{\theta} - \beta) + e_f \sin \hat{\theta}) - \frac{J_2 \sin^2 \hat{i}}{\hat{a}} \cos(2\hat{\theta}). \quad (30)$$

Thus, to find $\hat{\theta}^*$ and β^* , which are the candidates for the extremal points, one needs to solve:

$$0 = -\hat{a}e_p \sin(\hat{\theta}^* - \beta^*), \quad (31)$$

$$0 = \hat{a} (e_p \sin(\hat{\theta}^* - \beta^*) - e_f \cos \hat{\theta}^*) - \frac{J_2 \sin^2 \hat{i}}{2\hat{a}} \sin(2\hat{\theta}^*). \quad (32)$$

First, from Eq. (31), $\hat{\theta}^* = \beta^*$ or $\hat{\theta}^* = \pi + \beta^*$. Both cases lead, when replaced in Eq. (32), to the following equation:

$$0 = -\hat{a}e_f \cos \hat{\theta}^* - \frac{J_2 \sin^2 \hat{i}}{2\hat{a}} \sin(2\hat{\theta}^*) = -\cos(\hat{\theta}^*) \left[\hat{a}e_f - \frac{J_2 \sin^2 \hat{i}}{\hat{a}} \sin(\hat{\theta}^*) \right], \quad (33)$$

where the expansion of the sine of a double angle has been taken into account. Thus, the possibility $\cos(\hat{\theta}^*) = 0$ is considered first, leading to $\hat{\theta}^* = \pi/2$ or $\hat{\theta}^* = -\pi/2$.

Note there is also an additional critical point, namely the values of $\hat{\theta}^*$ making $\hat{a}e_f - \frac{J_2 \sin^2 \hat{i}}{\hat{a}} \sin(\hat{\theta}^*) = 0$. If $\left| \frac{\hat{a}^2 e_f}{J_2 k} \right| > 1$ there are no such solutions; exploring these values by replacing the formula $e_f \approx -\frac{J_3}{2J_2} \frac{\sin \hat{i}}{\hat{a}}$ in Eq. (33), one reaches

$$\frac{\hat{a}^2 e_f}{J_2 k} = -\frac{\hat{a} J_3}{2 J_2 \sin \hat{i}}, \quad (34)$$

which is a large number for LEO unless one is very close to an equatorial orbit, then one can replace $\sin \hat{i} \approx \hat{i}$ and gets the approximate inequality: $\hat{i} < \frac{\hat{a} J_3}{2 J_2}$ (taking $\hat{a} \approx 1$ and since $J_3/J_2 \approx 2 \cdot 10^{-3}$, $\hat{i} < 10^{-3}$ in radians, which is about 0.06 degrees). Thus, this solution is not taken into consideration in what follows.

Therefore, there are four candidates to be the critical points:

$$(\beta^*, \hat{\theta}^*) = \{(\pi/2, \pi/2), (-\pi/2, \pi/2), (-\pi/2, -\pi/2), (\pi/2, -\pi/2)\} \quad (35)$$

Computing now the Hessian H ,

$$H(\beta, \hat{\theta}) = \begin{bmatrix} \hat{a} e_p \cos(\hat{\theta} - \beta) & -\hat{a} e_p \cos(\hat{\theta} - \beta) \\ -\hat{a} e_p \cos(\hat{\theta} - \beta) & \hat{a} (e_p \cos(\hat{\theta} - \beta) + e_f \sin \hat{\theta}) - \frac{J_2 k}{\hat{a}} \cos(2\hat{\theta}) \end{bmatrix} \quad (36)$$

One has to remember that a critical point would be a saddle point if there is no sign definiteness. To have sign definiteness, it is required that the determinant of the Hessian is positive. Now, the determinant can be obtained as

$$\det(H) = \hat{a} e_p \cos(\hat{\theta} - \beta) \left(\hat{a} e_f \sin \hat{\theta} - \frac{J_2 \sin^2 \hat{i}}{\hat{a}} \cos(2\hat{\theta}) \right) \quad (37)$$

and, at the critical points, the situation is as follows

$$H(\pi/2, \pi/2) = \begin{bmatrix} \hat{a} e_p & -\hat{a} e_p \\ -\hat{a} e_p & \hat{a} (e_p + e_f) \end{bmatrix}, \quad \det(H) = \hat{a}^2 e_p e_f \quad (38)$$

$$H(-\pi/2, \pi/2) = \begin{bmatrix} -\hat{a} e_p & \hat{a} e_p \\ \hat{a} e_p & \hat{a} (-e_p + e_f) \end{bmatrix}, \quad \det(H) = -\hat{a}^2 e_p e_f \quad (39)$$

$$H(-\pi/2, -\pi/2) = \begin{bmatrix} \hat{a} e_p & -\hat{a} e_p \\ -\hat{a} e_p & \hat{a} (e_p - e_f) \end{bmatrix}, \quad \det(H) = -\hat{a}^2 e_p e_f \quad (40)$$

$$H(\pi/2, -\pi/2) = \begin{bmatrix} -\hat{a} e_p & \hat{a} e_p \\ \hat{a} e_p & \hat{a} (-e_p - e_f) \end{bmatrix}, \quad \det(H) = \hat{a}^2 e_p e_f \quad (41)$$

The conclusions depend on the sign of e_f . Normally, for geocentric orbits, since $e_f \approx -\frac{J_3}{2J_2} \frac{\sin \hat{i}}{\hat{a}}$ positive e_f can be

expected due to the negative sign of J_3 . Thus, $(\beta^*, \hat{\theta}^*) = \{(\pi/2, \pi/2), (\pi/2, -\pi/2)\}$ are the only points not leading to a saddle point. Both have $\beta = \pi/2$ which implies $\hat{\omega} = 90$, this is, being at the top of Cook's circle with $\hat{e} = e_p + e_f$. Then, the maximum is obtained at $\hat{\theta} = -\pi/2$ (minimum latitude point, being at the mean apogee) and the minimum is obtained at $\hat{\theta} = \pi/2$ (maximum latitude point, being at the mean perigee). Thus the space-occupancy results are reconstructed, obtaining Eq. (13) and (14) without the need of using frozen orbits.

In the unusual (but possible) case of $e_f < 0$, these results change. The extrema then happen at $\beta = -\pi/2$ which implies $\hat{\omega} = -90$, this is, being at the bottom of Cook's circle with $\hat{e} = e_p - e_f$. Then, the maximum is obtained at $\hat{\theta} = \pi/2$ (maximum latitude point, being at the mean apogee) and the minimum obtained at $\hat{\theta} = -\pi/2$ (minimum latitude point, being at the mean perigee)

Consider now the case under study (short-term space occupancy) in which β is confined to some values, namely $\beta \in [\alpha, \alpha + \tau_F k]$. For simplicity, denote the interval as $\beta \in [\beta_0, \beta_1]$. In what regards β , from calculus there are two possibilities: either the global critical points previously found are inside $\beta \in [\beta_0, \beta_1]$ (and then they are the global maximum / minimum), or, the extrema lie at the limits of the interval. Assuming $e_f > 0$ (the modifications for $e_f < 0$ are straightforward), this is an easy check: if $\pi/2 \in [\beta_0, \beta_1]$ then the extrema are the same found for the long-term; evidently, if they were global extrema for the full interval, they still are global for a problem in a shorter interval. Otherwise, the limits of the interval must be tested to find the one that contains the extrema.

At each of the limits of the interval, one replaces the value of β and the problem becomes finding the extrema of a function of a single variable ($\hat{\theta}$) as follows

$$\hat{r}(\hat{\theta}) \approx \hat{a} (1 - e_p \cos(\hat{\theta} - \beta_i) - e_f \sin \hat{\theta}) + \frac{J_2}{4\hat{a}} [(9 + \cos(2\hat{\theta})) \sin^2 \hat{i} - 6], \quad (42)$$

and finding the derivative of \hat{r} and equating it to zero to find the critical points $\hat{\theta}^*$

$$0 = \hat{a} (e_p \sin(\hat{\theta}^* - \beta_i) - e_f \cos \hat{\theta}^*) - \frac{J_2 k}{2\hat{a}} \sin(2\hat{\theta}^*), \quad (43)$$

for both $i = 1, 0$; the resulting values of \hat{r} evaluated at all possible critical points for β_1 and β_0 are then compared to see which one is the maximum and which one is the minimum.

It is important to notice that Eq. (43) can be reduced to a polynomial, which helps not only finding its solutions but also to precisely determine the number of possible critical points.

The classical change $x = \tan \hat{\theta}^*/2$, is bi-univocal between \mathbb{R} and $(-\pi, \pi)$; it implies $\cos \hat{\theta}^* = \frac{1-x^2}{1+x^2}$ and $\sin \hat{\theta}^* = \frac{2x}{1+x^2}$. After some manipulation,

$$0 = \hat{a} \left(e_p \frac{2x}{1+x^2} \cos(\beta_i) - e_p \frac{1-x^2}{1+x^2} \sin(\beta_i) - e_f \frac{1-x^2}{1+x^2} \right) - \frac{J_2 k}{\hat{a}} \frac{2x(1-x^2)}{(1+x^2)^2} \quad (44)$$

and cross multiplying (44) by $(1+x^2)^2$ gives the fourth-order polynomial (quartic)

$$0 = -(\hat{a}e_p \sin(\beta_i) + \hat{a}e_f) + 2x \left(\hat{a}e_p \cos(\beta_i) - \frac{J_2 \sin^2 \hat{i}}{\hat{a}} \right) + 2x^3 \left(\hat{a}e_p \cos(\beta_i) + \frac{J_2 \sin^2 \hat{i}}{\hat{a}} \right) + x^4 (\hat{a}e_p \sin(\beta_i) + \hat{a}e_f), \quad (45)$$

which should have exactly four solutions that can be efficiently computed as roots of a polynomial, and then undo the change of variables.

Notice Eq. (45) can be written in terms of the eccentricity vector at β_i , since $\xi_i = e_p \cos(\beta_i)$, $\eta_i = e_p \sin(\beta_i) + e_f$; then one has:

$$0 = -1 + x \left(2 \frac{\hat{a}^2 \xi_i - J_2 \sin^2 \hat{i}}{\hat{a}^2 \eta_i} \right) + x^3 \left(2 \frac{\hat{a}^2 \xi_i + J_2 \sin^2 \hat{i}}{\hat{a}^2 \eta_i} \right) + x^4 \quad (46)$$

or, if one recalls $\xi = \hat{e} \cos \hat{\omega}$ and $\eta = \hat{e} \sin \hat{\omega}$, and denotes by \hat{e}_i and $\hat{\omega}_i$ the values of mean eccentricity and argument of perigee at the beginning and end of the interval,

$$0 = -1 + x \left(2 \frac{\hat{a}^2 \hat{e}_i \cos \hat{\omega}_i - J_2 \sin^2 \hat{i}}{\hat{a}^2 \hat{e}_i \sin \hat{\omega}_i} \right) + x^3 \left(2 \frac{\hat{a}^2 \hat{e}_i \cos \hat{\omega}_i + J_2 \sin^2 \hat{i}}{\hat{a}^2 \hat{e}_i \sin \hat{\omega}_i} \right) + x^4 \quad (47)$$

In addition, the possibility of a root at infinity has to be taken into account. Taking limit in the polynomial Eq. (44) before cross-multiplying it by $(1+x^2)^2$, it can be seen that this only happens if $e_p \sin(\beta_i) + e_f = \eta_i = \hat{e}_i \sin \hat{\omega}_i = 0$ (or in other words, when $\hat{\omega}_i = 0, \pi$), which in fact implies the two solutions $x = 0, \infty$, this is, $\hat{\theta}^* = 0, \pi$.

Indeed, when $\sin \hat{\omega}_i \neq 0$ the quartic can be rewritten in the more compact form:

$$x^4 + Px^3 + Qx - 1 = 0 \quad (48)$$

with:

$$P = \frac{2\hat{a}^2 \hat{e}_i \cos \hat{\omega}_i + 2J_2 \sin^2 \hat{i}}{\hat{a}^2 \hat{e}_i \sin \hat{\omega}_i} \quad Q = \frac{2\hat{a}^2 \hat{e}_i \cos \hat{\omega}_i - 2J_2 \sin^2 \hat{i}}{\hat{a}^2 \hat{e}_i \sin \hat{\omega}_i}$$

The space occupancy quartic equation admits up to four real solutions that can be found analytically (using Ferrari's method) or with an efficient numerical approach (e.g. using Newton's or Halley's method).

Both the radius and the second derivative (to verify the character of the critical point) can be expressed in terms of x , so there is no need, in fact, to undo the change of variables

$$\hat{r} = \hat{a} \left(1 - \hat{e}_i \frac{(1-x^2) \cos \hat{\omega}_i - (2x) \sin \hat{\omega}_i}{1+x^2} \right) + \frac{J_2}{4\hat{a}} \left[\left(9 + \frac{1-6x^2+x^4}{(1+x^2)^2} \right) k - 6 \right], \quad (49)$$

$$\frac{\partial^2 \hat{r}}{\partial \hat{\theta}^2} = \hat{a} \hat{e}_i \frac{(1-x^2) \cos \hat{\omega}_i - (2x) \sin \hat{\omega}_i}{1+x^2} - \frac{J_2 k}{\hat{a}} \frac{1-6x^2+x^4}{(1+x^2)^2}. \quad (50)$$

C. Short-term space occupancy validation

Next, the results of Section II.B are numerically validated with a high-fidelity propagator.

Figure 4 shows the effectiveness of the short-term space occupancy formulation. This figure presents the bounding envelopes resulting from the solution of the polynomial of Eq. (48), overlaid with the corresponding numerically propagated radius evolution for three test cases over their J_2 -induced line of apsides precession period. Figure 4(a) corresponds to the orbit with NORAD 47961; with an initial osculating inclination of 97.51 degrees and initial osculating eccentricity equal to $3.11e^{-3}$. Figure 4(b) represents the case of the orbit with NORAD 41460; with an initial osculating inclination of 98.27 degrees and an initial osculating eccentricity of $1.25e^{-2}$. Finally, data shown in Fig. 4(c) are from the orbit with NORAD 43518; with an initial osculating inclination of 35.08 degrees and initial osculating eccentricity of $5.07e^{-4}$.

These orbits have been propagated with a high-fidelity model, including 23×23 geopotential model, lunisolar third body perturbation and Earth's geoid precession, nutation, and polar motion.

On the other hand, in order to compute the evolution of the short-term space occupancy for each of these orbits, the mean orbital elements have been calculated from the initial conditions. Using these values, the coefficients P and Q have been obtained at each time. Afterward, Eq. (48) has been solved, finding the critical points and obtaining the evolution of the radius extremes by Eq. (49). The *frozen eccentricity* used in the computations was obtained employing Eq. (5) up to fifteenth degree. The mean orbital elements have been derived using Kozai [19] and Lyddane equations [20] (which only includes first-order J_2 terms) as reported in the Appendix for convenience.

These graphics show a good fit between the short-term space occupancy estimates and the radius evolution contour. However, it is important to take into account that the short-term study of space occupancy equations has been motivated by much shorter screening time horizons. Thus, Fig. 5 shows the short-term space occupancy computed within a 5-days time window (a typical horizon for conjunction screening) that moves throughout the complete line of apsides precession period, for the same orbits of Fig. 4. In this case, for the purposes of the short-term space occupancy, the mean orbital elements have been computed at each instant of time whereas β^* is computed as explained in Section II.B every 5 days, thus obtaining the upper and lower limits of the radius for that 5-day period.

It can be noticed that the short-term space occupancy error has considerable changes as time evolves and is highly dependent on the orbit under study. In order to better analyze the accuracy of the 5-day short-term space occupancy, a total population of real orbits obtained from TLEs has been considered. In particular, a sample of 16 972 orbits has been constructed by considering all cataloged objects whose last TLE data were after 10/24/2022 and removing those with apogee radii close to 40 000 km or greater and eccentricity close to 0.1 or greater. The corresponding TLEs have been retrieved from the Space-Track on 11/04/2022.

Taking as the error of each case the largest difference over the J_2 -induced line of apsides precession period, Fig. 6 presents the distribution of this error and its cumulative density function. The mean error is around 0.5 kilometers,

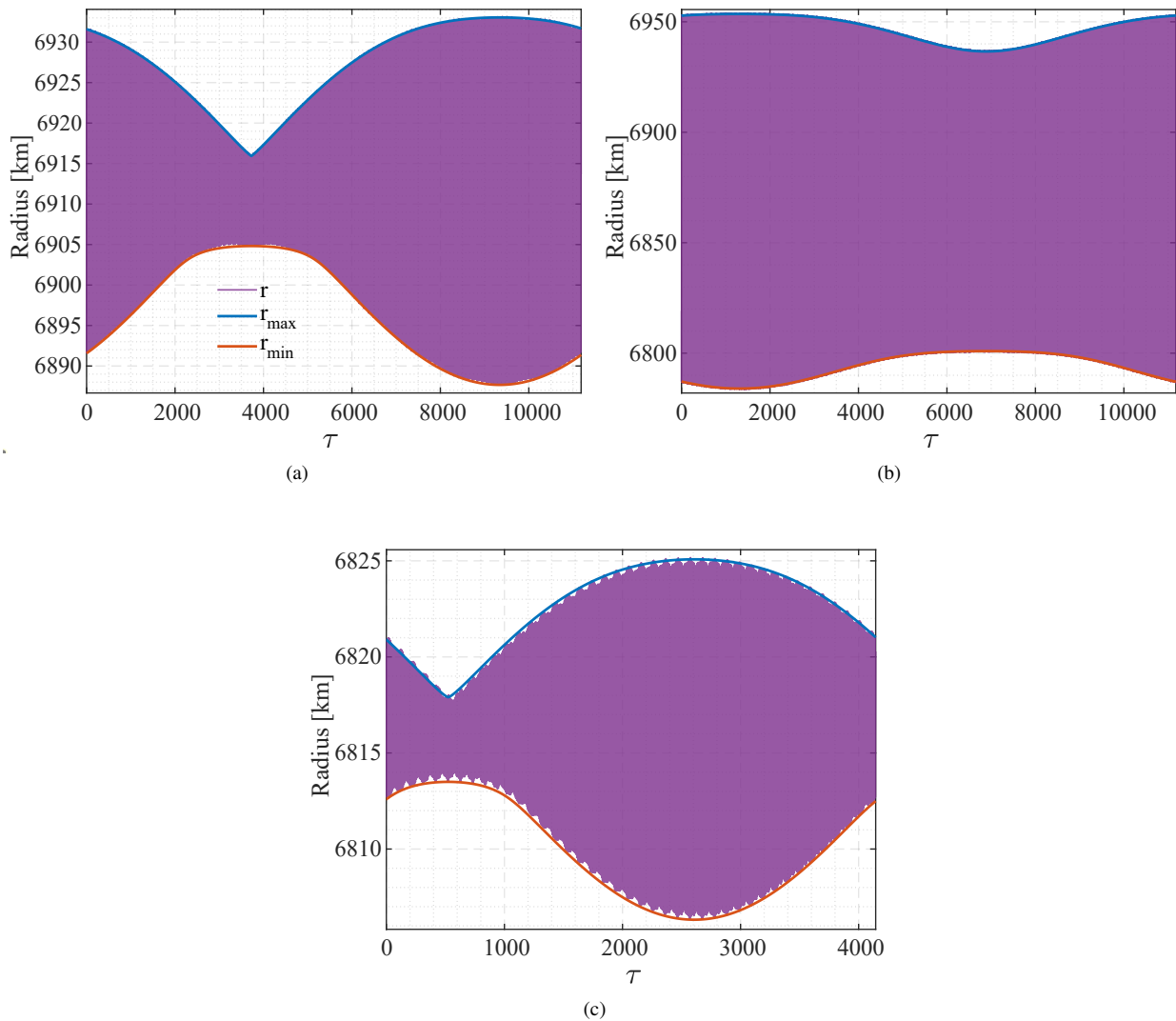


Fig. 4 Short-term space occupancy bounding for NORAD 47961 (a), NORAD 41460 (b) and NORAD 43518 (c).

which can be considered sufficiently accurate considering that the uncertainty of the initial data, taken from the TLEs, is greater. In fact, 98.7% of the samples have an error of less than one kilometer.

III. Space Occupancy Conjunction Filter

As argued in Section I, the implementation of filtering mechanisms to exclude pairs of RSOs with no possible collision is among the most prevalent strategies utilized to expedite conjunction computations [11, 21]. One of the main drivers of this work is the use of space occupancy to develop new filters. Thus, starting from the radial bounds equations developed in Section II.B, a novel space occupancy conjunction filter (SO-filter) that aims to replace and improve the classical AP-filter has been implemented and tested. Improving the performance of the AP-filter, which serves as the

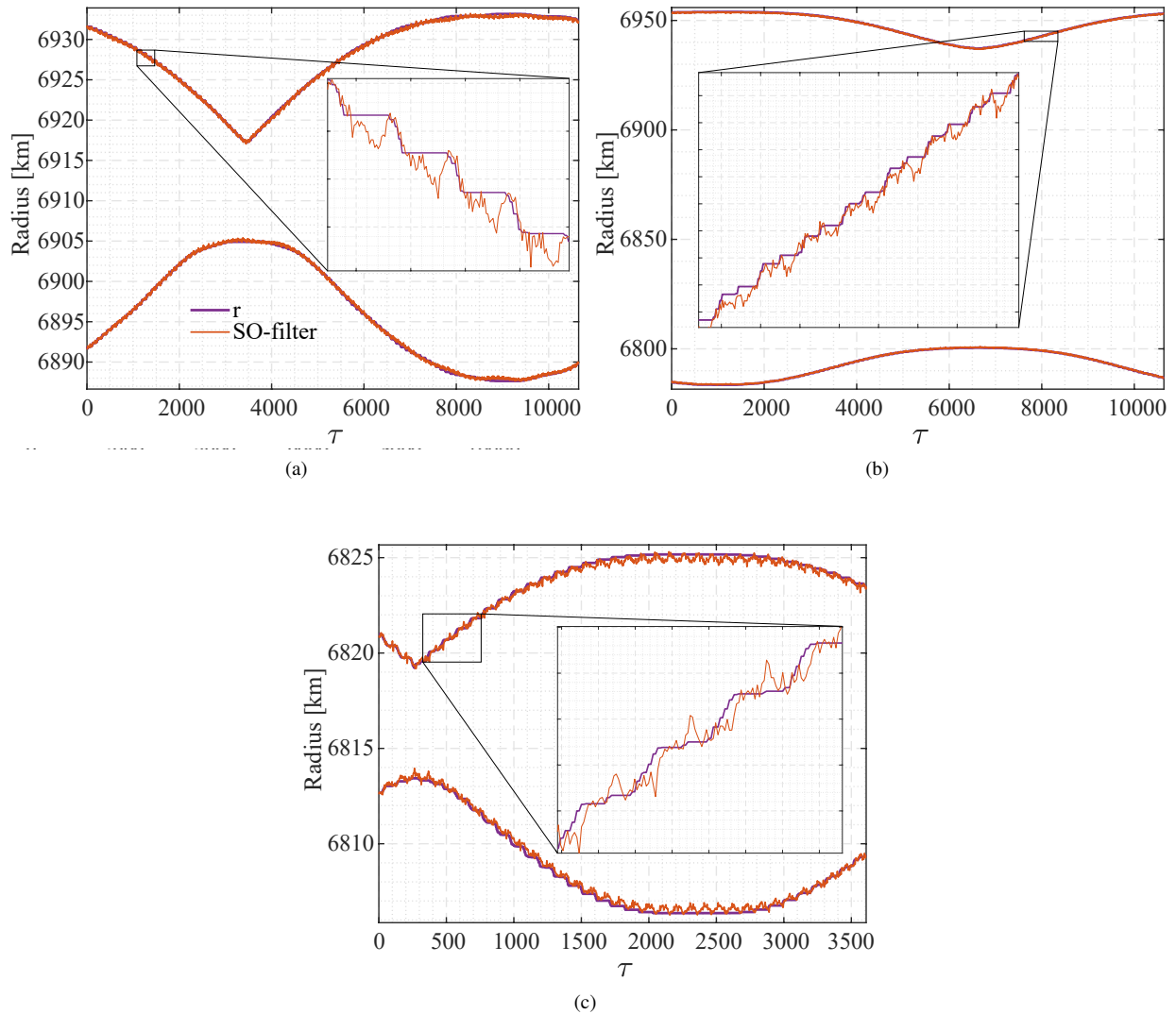


Fig. 5 5-day short-term space occupancy bounding for NORAD 47961 (a), NORAD 41460 (b) and NORAD 43518 (c).

initial filtering stage in systems like GMV's "Smart Sieve" [22], can consequently even enhance the efficacy of more complex filtering algorithms.

The performance of the SO-filter has been compared with the following filters:

- 1) The classical AP-filter [12].
- 2) The accurate but time-consuming solution of the short-time space occupancy problem obtained by from the resolution of Eq. (17) (finding the extrema with respect to time), denoted as "SO-filter exact." Note that this procedure is much slower than just solving the quartic (48).
- 3) The filter developed in [23], which is based on a simple but conservative approximation, according to the idea of bounding separately the two brackets of Eq. (16) by their respective extrema. In what follows this filter is

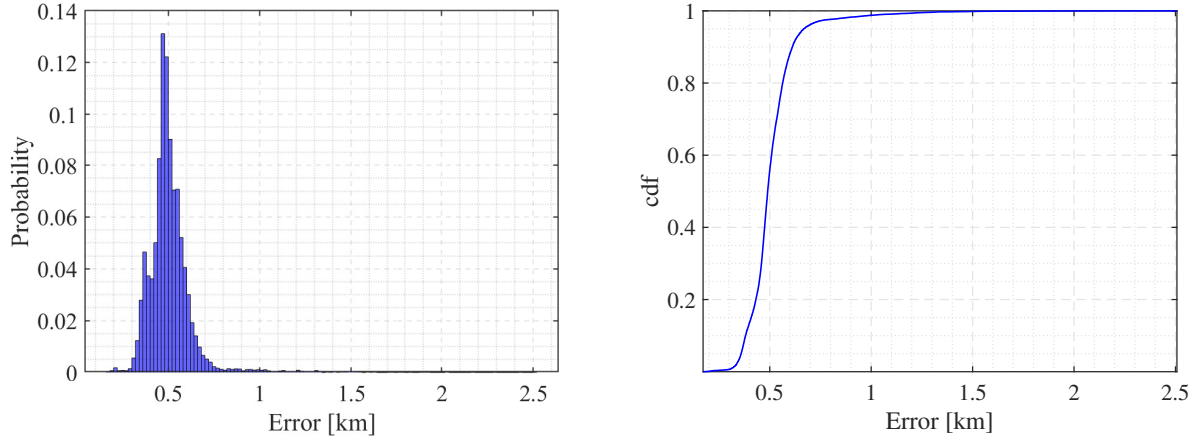


Fig. 6 Short-term space occupancy error histogram (left) and cumulative density function (right).

denoted as the space occupancy *simplified* filter, or “SOS-filter” for short.

To test and compare the filters, as in Section II.C, the osculating orbital elements initial conditions of all cataloged RSOs with their last TLE data between 10/24/2022 and 11/04/2022 (removing those orbits with a maximum radius close to 40 000 km or greater and an eccentricity close to 0.1 or greater) have been considered after downloading and processing Two-line Elements (TLEs) data based on SGP4 theory [24]. This set of orbits provides a total of 144.02 million pairs to analyze. These elements have been propagated to a common initial instant t_0 (11/02/2022 09:18:20) with a high-fidelity model, including 23×23 geopotential model, lunisolar third body perturbation and Earth’s geoid precession-nutation and polar motion. Then, the corresponding mean orbital elements have been derived using Kozai-Lyddane equations*.

Next, the filters are initially compared in Section III.A without the inclusion of buffers. However, it is well-known that buffers are necessary to improve the performance of the filters [14]. Buffers are thus next obtained and the buffered filters are then compared in Section III.B. Finally, the effect of the atmospheric drag is considered in Section III.C.

A. Comparison of filters without buffer

A simple and preliminary comparison of the filter performance considering the new SO-filter, the SOS-filter, the SO-filter exact, and the classical AP-filter has been conducted without considering any buffer, between t_0 and t_0 plus five days. In this comparison, a “positive” result is considered when a pair of orbits has an overlapping range of radii (note that this not implies that there is a collision, only that it cannot be discarded so further analysis would be necessary). A “negative” result is obtained when the radii can never overlap (and therefore a collision is impossible). The high-fidelity propagator is used to obtain “true” results for the purpose of comparison by obtaining the range of radius along 5 days. Note that atmospheric drag has not been included in the propagator in this analysis. The effect of this perturbation is

*Note that implementing the filter based on the average orbital elements extracted directly from the TLEs provided considerably worse performance.

analyzed in Section III.C.

Given two orbits i and j , each filter excludes the pair (i, j) when one of the next two conditions are met:

$$\begin{aligned} r_{max,i} &< r_{min,j} \\ r_{max,j} &< r_{min,i} \end{aligned} \tag{51}$$

otherwise, the pair is kept. In Eq. (51), r_{max} and r_{min} are computed by each particular filter. Specifically, for the AP-filter the mean apogee and perigee at the reference time t_0 was used, since using the osculating apogee and perigee radii was seen to deteriorate the filter performance. This can be appreciated in Fig. 3, where it can be observed that the osculating apogee and perigee are highly time-dependent.

Table 1 summarizes the results of the four filters, including the number of false positives, false negatives, precision (percentage of real positives detected among all positives detected by the filter), and recall (percentage of real positives detected among all real positives).

Table 1 Summary of Filter Performance Comparison, without buffer.

Filter	False Positives	False Negatives	Precision	Recall
SO-filter	2 296	65 355	99.993%	99.795%
AP-filter	224 312	537 201	99.291%	98.319%
SO-filter exact	1 889	67 054	99.994%	99.790%
SOS-filter	445 342	6 752	98.625%	99.979%

First of all, it should be noted that the performance of the SO-filter and the SO-filter exact is quite similar, even though the latter is much more computationally intensive. In relation to the false positives, the conservative character of the SOS-filter makes it perform even poorer than the AP-filter whereas the SO-filter manages to reduce them by two orders of magnitude. On the other hand, both SOS-filter and SO-filter considerably reduce the number of false negatives compared to the AP-filter with a very notorious decrease in the SOS-filter due to its conservativeness (this is, this number is small at the expense of the large number of false positives).

Indeed, Fig. 7 shows the distribution of the error in radial distance for the 16972 orbits, computed as the maximum radius minus the upper bound (in Fig. 7(left)) or the lower bound minus the minimum radius (in Fig. 7(right)) for both SOS-filter and SO-filter. This magnitude is negative when the boundary overestimates the radius, resulting in false positives. It can be noticed that the modes of the distributions are the same for both filters (between 0 and 0.1 for both maximum and minimum). However, the dispersion of the SOS-filter towards negative values, due to its conservativeness, is much larger than that of the SO-filter, which explains the difference in the number of false positives.

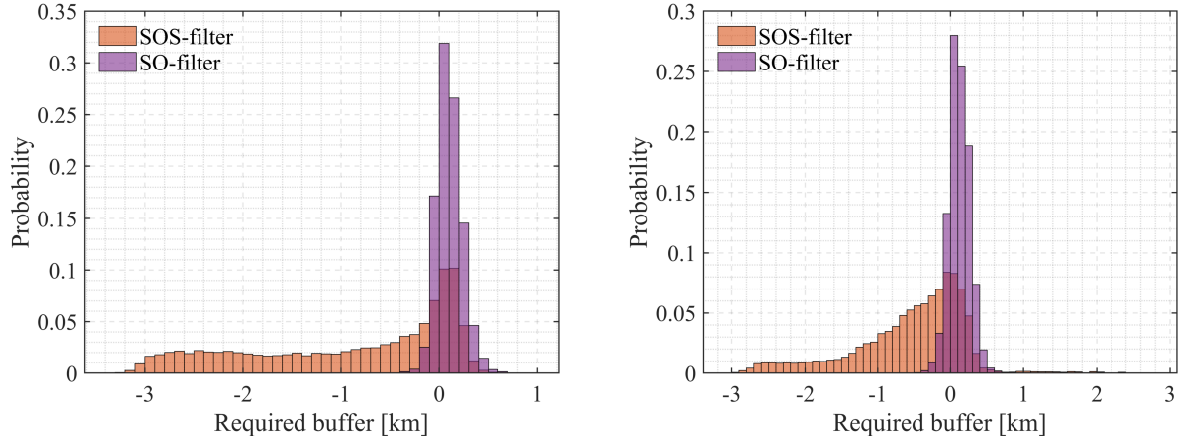


Fig. 7 Histogram of bounding errors at maximum radius (left) and minimum radius (right).

B. Comparison of filters with buffer

In conjunction analysis, filters with false negatives are not acceptable since they might imply that some potential collisions are not further investigated, whereas false positives, while harmful, are acceptable: they should (ideally) be reduced to diminish computation times, but they only imply that more pairs are kept for further analysis. To eliminate false negatives, *buffers* are used to ensure that the filters correctly bound the orbits even at the expense of some additional conservativeness that increases false positives.

As seen in Section II.C, the errors in computing the radius extremes are not the same throughout the line of apsides precession period, being highly dependent on the initial point. Therefore, to obtain the correct buffers that do not depend on the specific time horizon under study, the radii evolution have been computed over the line of apsides precession period (except for those orbits for which this time interval exceeded one year, for which the evolution has been calculated over 365 days) using the high-fidelity propagator described in Section II.C, and they have been compared to the corresponding bounds predicted by each filter. For each orbit, the maximum excess radial distance over this period was recorded and the maximum of all these distances was set up as the model error buffer, b .

Figure 8 and Fig. 9 present the histogram and the cumulative density function of the buffer needed for the four filters, for the 16972 orbits, focusing only in positive errors. Figure 8 correspond to the given initial conditions ($t_0 = 11/02/2022$ 09 : 18 : 20) and Fig. 9 refers to the maximum buffer computed by varying the initial conditions over a complete J_2 -induced line of apsides precession period. It can be seen that the behavior is similar; however, taking the maximum over a precession period moves the histogram to the right, increasing the buffers.

Those plots allow a quick comparison of the error of each filter. It can be noticed in Fig. 8 that, while most orbits require a buffer between 3-6 km with the AP-filter, the aforementioned SO-filter and SOS-filter distribution modes are between 0.1 and 0.2 km, as well as the mode of the distribution corresponding to the SO-filter exact. Furthermore, Fig. 8 shows that to achieve a proper bounding of all the orbits of the population, the AP-filter requires a buffer of 10.722 km

while the SO-filter and SOS-filter, require a buffer of 1.119 km and 2.730 km, respectively. It is important to point out that with the SO-filter exact, this maximum would be equal to 1.118 km, essentially the same needed by the SO-filter.

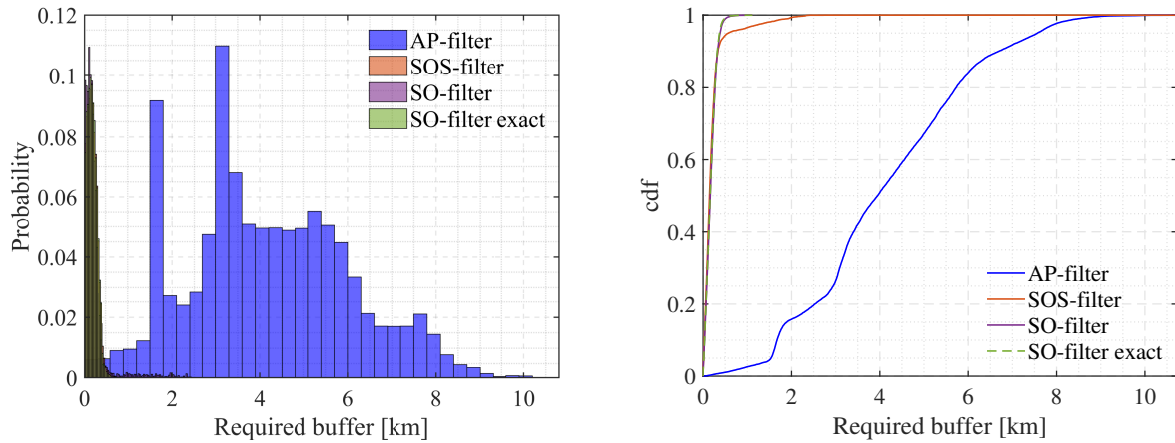


Fig. 8 Buffer histogram (left) and cumulative density function (right) for all filters.

Consider next the analysis over the complete J_2 -induced line of apsides precession period. Regarding the AP-filter, it is observed that, although the maximum increases by less than 10%, the maximum buffer is 11.527 km, most of the orbits increase their error to a value of around 8 km. In relation to the SO-filter, the SOS-filter, and the SO-filter exact, the three distributions shift roughly the same distance to the right and the modes are around 0.5-0.6 km. The buffers required to bound the population without any error are 3.347 km for the SOS-filter and 2.508 km for the SO-filter and the SO-filter exact.

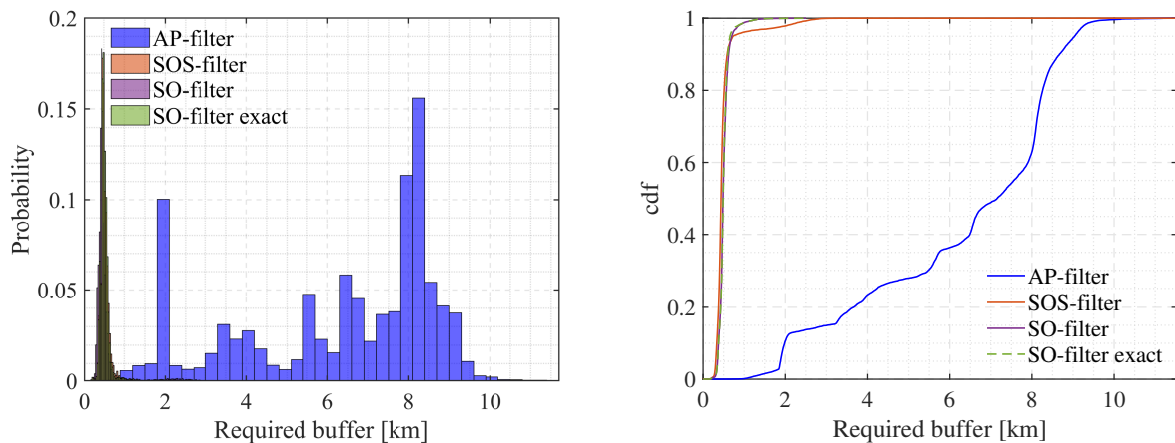


Fig. 9 Buffer histogram (left) and cumulative density function (right) over one precession period.

Considering the buffers, the filters now exclude from further conjunction assessment all pairs of satellites obeying

any of the two conditions:

$$\begin{aligned} r_{max,i} + b &< r_{min,j} - b \\ r_{max,j} + b &< r_{min,i} - b \end{aligned} \tag{52}$$

which makes them robust against false-negative type of errors, where the model error buffer chosen is the maximum determined by the analysis performed over the J_2 -induced line of apsides precession period.

Table 2 summarizes the results of the four filters when buffers are included. This table includes the number of false positives and precision because all false-negative type of error has been eliminated with the buffer. In addition, it shows the number of pairs that should be assessed further. The SOS-filter removes almost 4 million more than the AP-filter, resulting in a 10% reduction in the number of pairs that need further analysis. The SO-filter removes more than 4.5 million more than the AP-filter and practically the same number of pairs as with the SO-filter exact. The latter just eliminates about 2000 more pairs than the SO-filter, a very small improvement given the increased computational load.

Table 2 Summary of Filter Performance Comparison with the required buffer.

Filter	False Positives	Precision	Pairs to check after filter
SO-filter	1 300 029	96.090%	33 250 618
AP-filter	5 967 657	84.262%	37 918 246
SO-filter exact	1 298 306	96.095%	33 248 895
SOS-filter	2 263 547	93.384%	34 214 136

Furthermore, the fact that the maximum required buffer is five times greater than the mode of its distribution leads to the consideration of whether the few cases requiring a larger buffer share some common characteristics. Indeed, it has been observed that these few cases are more eccentric and higher altitude orbits. Therefore, in order to avoid penalizing the entire population with such a high buffer, it has been decided to divide the population into six distinct groups attending to minimum altitude and eccentricity and apply a characteristic buffer to each category, for each filter.

Regarding eccentricity, the population has been divided into two groups, considering orbits with an eccentricity less than 0.1 as low eccentricity orbits. Within the low eccentricity orbits, four categories have been distinguished based on minimum altitude: the first one with a minimum altitude below 400 km, the second group with a minimum altitude between 400 and 700 km, the third group between 700 and 1000 km, and finally, higher altitude orbits, including all those above 1000 km. On the other hand, orbits with higher eccentricities have been divided into two groups: low-altitude orbits with a minimum altitude below 1000 km, and high-altitude orbits comprising all others. Table 3 presents the required buffer for each filter and each category.

Table 4 summarizes the results of the four filters with their buffers presented in Table 3. It is important to highlight that this latest improvement represents a decrease of more than 50% in false positives for the SO-filter, removing almost 800 000 more pairs at a very small additional cost.

Table 3 Required buffer for each filter according to categories.

Eccentricity	Altitude [km]	SO-filter	AP-filter	SO-filter exact	SOS-filter
$e_m < 0.01$	$h_{min} < 400$	0.9782	11.5271	0.9780	1.2586
	$h_{min} < 700$	1.2823	11.2849	1.2827	3.3474
	$h_{min} < 1000$	0.7378	10.2531	0.7066	3.0379
	$h_{min} > 1000$	2.0260	8.5749	2.0263	2.8355
$e_m > 0.01$	$h_{min} < 1000$	0.9009	10.7209	0.9018	3.0047
	$h_{min} > 1000$	2.5072	8.4504	2.5076	2.7253

Table 4 Summary of Filter Performance Comparison with the required buffer.

Filter	False Positives	Precision	Pairs to check after filter
SO-filter	531 916	98.362%	32 482 505
AP-filter	5 507 984	85.296%	37 458 573
SO-filter exact	524 183	98.386%	32 474 772
SOS-filter	2 145 317	93.708%	34 095 906

To close the comparison between the filters, the behavior of false positives and false negative type of error with respect to the buffer size have been analyzed following the methods [14], which uses ratios instead of absolute values. The false positives rate is defined as the ratio of false positives to actual negatives and the false negative rate as the ratio of false negatives to actual positives.

Figure 10 shows that the false positive errors increase with the buffer size, as would be expected. SOS-filter and SO-filter have parallel behavior with respect to buffer size, but using the SO-filter results in fewer cases of false positives. The AP-filter presents intermediate results between the two filters for small buffers, but it improves the results of the SOS-filter and the SO-filter with buffers higher than 1 km.

Figure 11 presents the percentage of false negatives errors as a function of the buffer. The improvement of the SO-filter can be seen in this type of error. A buffer of 1.5 km or 1 km is enough to eliminate all these errors with the SOS-filter and SO-filter, respectively. However, the AP-filter requires a buffer of 9.5 km to achieve this goal.

Finally, Fig. 12, known as operating characteristic curve [25], presents true positive rates (ratio of true positives to actual positives, the same concept as precision) as a function of false positive rates. This type of curve is used to compare two operating characteristics and depicts relative trade-offs between benefits (true positives) and costs (false positives). This graph shows that an increase in false positives is associated with an increase in true positives. The performance of the filter is better the closer this curve is to the upper left corner. As is readily seen, the AP-filter has a significantly lower true positive rate than the SO-filters, reaching 100% of true positives with a much higher false positive rate than the other filter. These three graphs show again that the SO-filter has practically the same performance as the SO-filter exact at a much smaller computational cost.

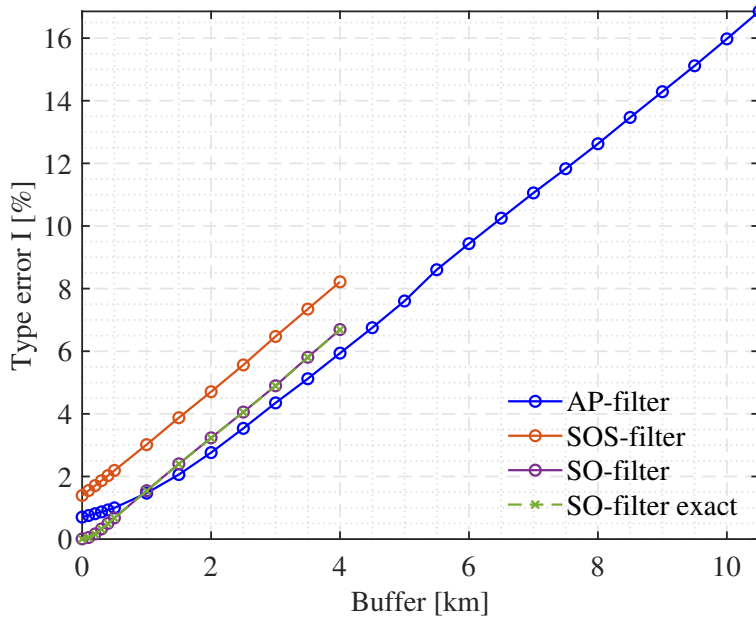


Fig. 10 False positives type of errors.

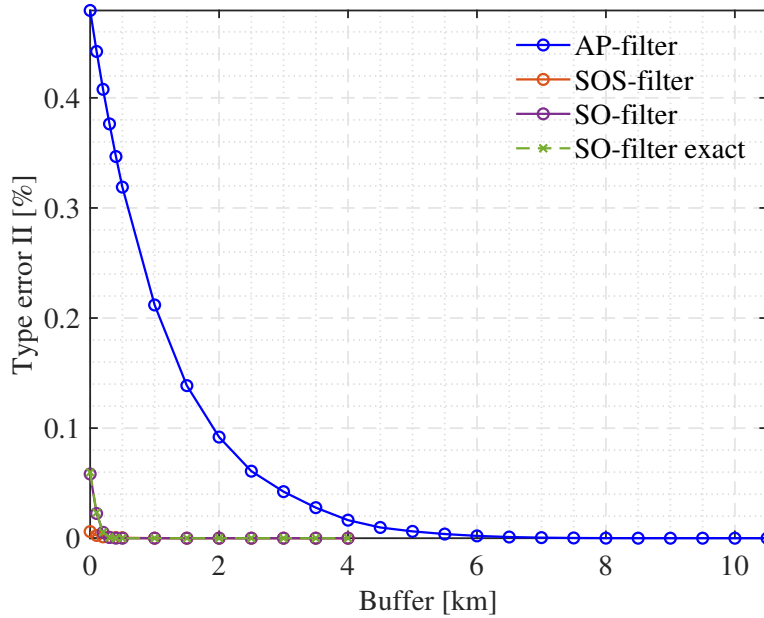


Fig. 11 False negatives type of errors.

C. Atmospheric drag

The previous results do not take into account the effect of atmospheric drag, which is relevant on low enough orbits. Thus, to analyze the influence of drag, its effect has been studied on objects of the population whose minimum altitude is less than 500 km. The impact of atmospheric drag on the minimum radius has been studied in the 5-day time interval

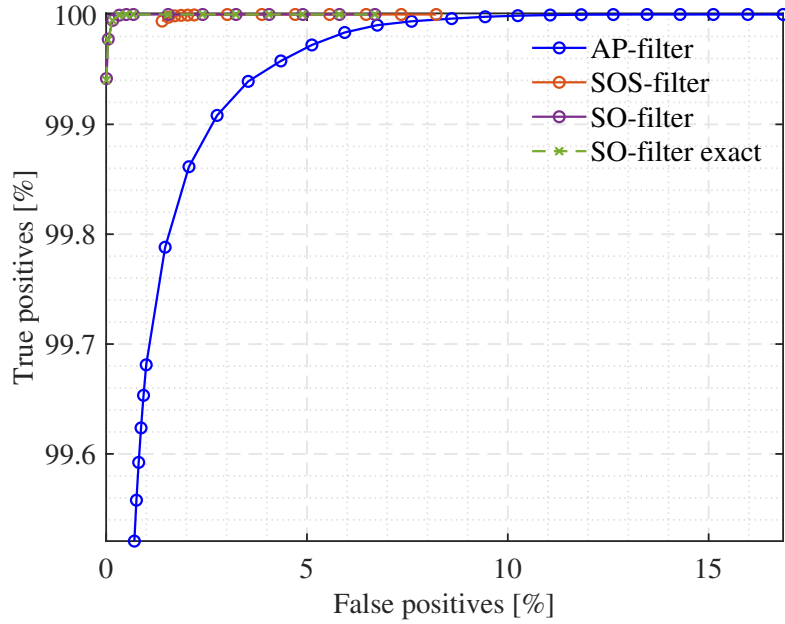


Fig. 12 Operating characteristic curve.

in which the filter is framed. The idea is to compute the decrease of the lower limit of the radius due to this perturbation with a simplified model that allows a quick estimation to be included in the filter estimates. In particular, the equation developed by Billik [26] has been employed to model the minimum radius descent, Eq. (53), which relates altitude variations to time.

$$h = \frac{1}{\beta_a} \log \left[e^{\beta_a h_0} - B \sqrt{\mu R_{\oplus}} \beta_a \bar{\rho} t \right] \quad (53)$$

where h_0 is the initial altitude, t is the time and B is the ballistic coefficient. This is defined by Eq. (54), where C_D is the satellite's drag coefficient, A_v is the area of the satellite perpendicular to the velocity vector and m_v is the satellite's mass.

$$B = \frac{C_D A_v}{m_v} \quad (54)$$

As the source of information used is from the TLE data, the ballistic coefficient is computed using the method developed by Hoots and Roehrich [27], which relates the ballistic coefficient to the B^* drag term of the TLEs. From Vallado [18] the ballistic coefficient and the B^* drag term are related, using this method, by Eq. (55).

$$B = 12.741621 B^* \quad (55)$$

For the atmospheric density an exponential model is assumed [18] and the constants β_a and $\bar{\rho}$ can be computed with

the fit of Eq. (56) [26]. A layer-technique (or multi-fit) has been employed to improve the result. The atmosphere has been divided into seven layers of 50 km starting at 125 km of altitude.

$$\rho = \bar{\rho}e^{-\beta_a h} \quad (56)$$

In order to test the reliability of this model, the radius evolution of the orbits whose altitude dropped below 500 km has been computed over 5 days with the high-fidelity model of Section II.C now including the atmospheric drag. The implementation of this perturbation utilizes the exponential atmospheric model as presented in [18] and computes the ballistic coefficient from the B^* drag term through Eq. (55). The decrease in altitude predicted by the model is compared with the difference between the minimum radii of the propagations with and without atmospheric drag. Figure 13 shows the difference between the minimum radius decay computed with the propagations and the decay computed by the model, for those cases where reentry is not achieved (considering reentry at altitudes below 150 km). It can be seen that, in general, the model overestimates the descent; there are only a few cases where the model predicts a lower descent than the real one. As this is a preliminary analysis to take into account the effect of this perturbation on the SO-filter, in order to avoid any false negative, a safety margin of 0.6 km have been added to ensure that the bounds used cover the entire space occupancy of the orbits, avoiding false negatives.

In those cases where the model predicts reentry, the minimum radius has been set to 0, since the study of reentry is out of the scope of this analysis.

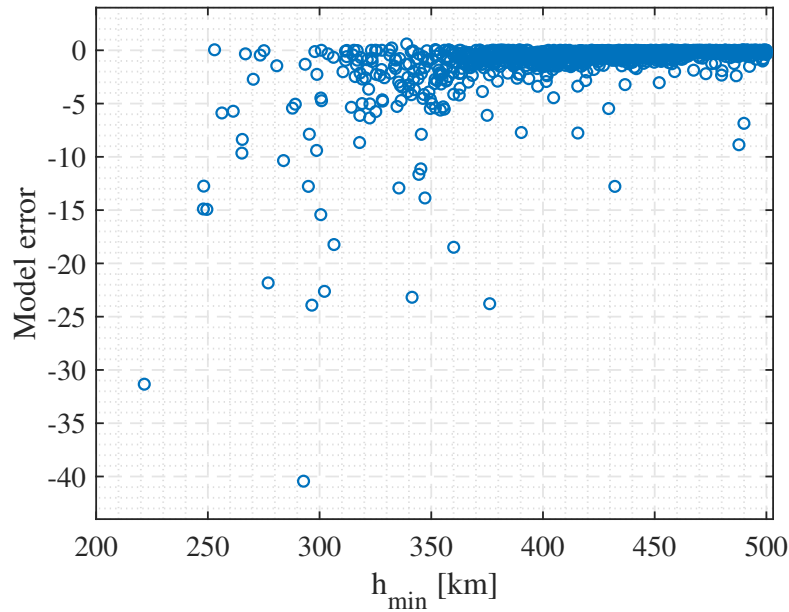


Fig. 13 Model error with respect to the minimum real altitude.

To analyze and compare the performance of the SO-filter, taking into account the atmospheric drag, the analysis

performed previously on the population of 16972 orbits has been reproduced. In this case, after adding the model error buffer, it is checked whether the lower bound is below 500 km altitude. If this is the case, the lower bound is modified to cover the effect of atmospheric drag. The altitude drop due to this perturbation is computed by Eq. (53), taking as initial altitude the one corresponding to the TLE data. Then, the lower bound is reduced by this amount and reentry condition is checked. If the minimum altitude is below 150 km, reentry is considered and the lower bound is set to 0 km.

Table 5 Summary of Filter Performance Comparison including atmospheric drag.

Filter	False Positives	Precision	Pairs to check after filter
SO-filter	545 681	98.321%	32 496 270
AP-filter	5 520 894	85.266%	37 471 483
SO-filter exact	537 930	98.344%	32 488 519
SOS-filter	2 158 894	93.671%	34 109 483

The performance results of the four filters have been recomputed with these new bounds and taken as true bounds those obtained from the propagations including atmospheric drag. Table 5 shows the summary of these results. As Table 2, it includes the number of false positives, precision, and the number of pairs that should be assessed further. Note that the precision decreases concerning the previous analysis, but only by 0.03-0.04%, and by approximately the same amount for the 4 filters. The atmospheric drag affects the same way the four filters, maintaining the conclusions of Section III.B.

IV. Space Traffic Management Analysis

This last section includes a brief analysis of the evolution of the space population from 2005 to the present using the space occupancy tools developed in this work. The data set of this analysis has been downloaded from the cloud storage site of Space Track. Starting at 2005, the number of cataloged objects for each year has been established by adding the cataloged objects for the month of January. Figure 14 shows the evolution of the total population over the years and the evolution of the population in which the SO-filter can be applied, orbits with apogee radii close to 40 000 km or greater and eccentricity close to 0.1 or greater.

As is already known, the number of objects in space has been rapidly increasing, as can be seen in Fig. 14. However, the number of objects sharing their space occupancy has not evolved in the same way. Figure 15 shows the total number of pairs, which could produce potential collisions, for each year, and the number of pairs that do not pass the SO-filter, i.e., the number of pairs that shares space occupancy. The number of pairs sharing space occupancy is initially increasing until 2010, thereafter, although the population and the total number of pairs are increasing, those that share space occupancy remain more or less constant. Thus, while in 2010 40% of pairs shared space occupancy, in 2021 this percentage is 26% and in 2022 is just 23%. This has resulted in better management of space. However, it is important to highlight the increase in the number of these couples sharing space in the last year, mainly due to the launch of the new

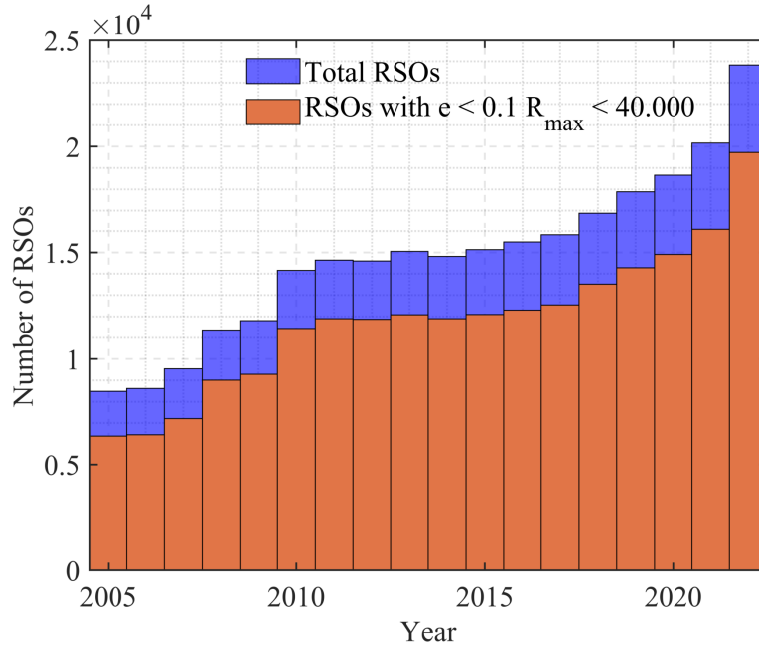


Fig. 14 Evolution of the space population from 2005 to the present.

megaconstellations.

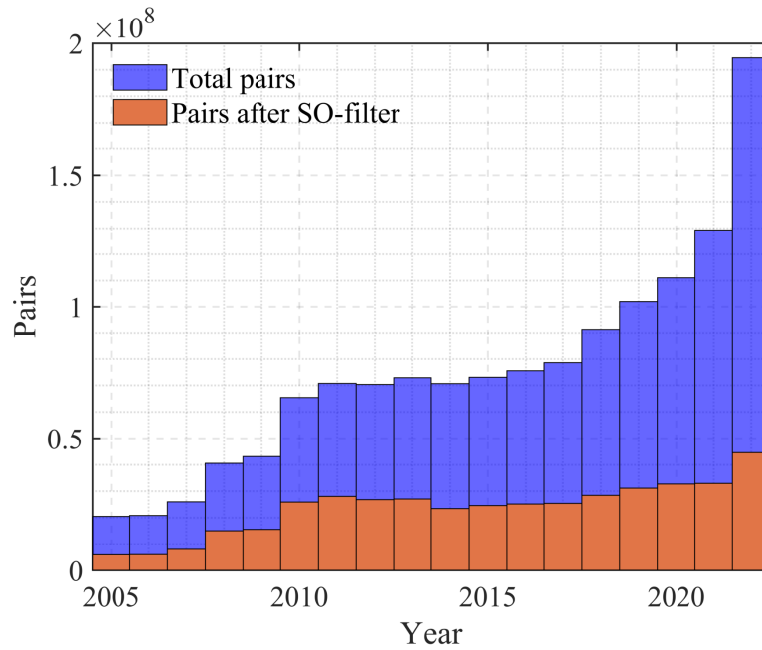


Fig. 15 Evolution of space distribution from 2005 to the present.

In addition, the number of neighbors of each object has been studied, understanding as neighbors of one object those orbits that share space occupancy with it. Figs. 16(left) and 16(right) show the histograms of the number of neighbors in 2005 and 2022, respectively. As was seen in Fig. 14, the space population from 2005 until now has multiplied its

size by 2.5. Therefore, the increase in the number of neighbors per orbit is natural. It can be noticed how the largest neighborhoods have tripled in size and how most of the orbits in 2005 had around 1500 neighbors, while now it is between 2000-4000 neighbors.

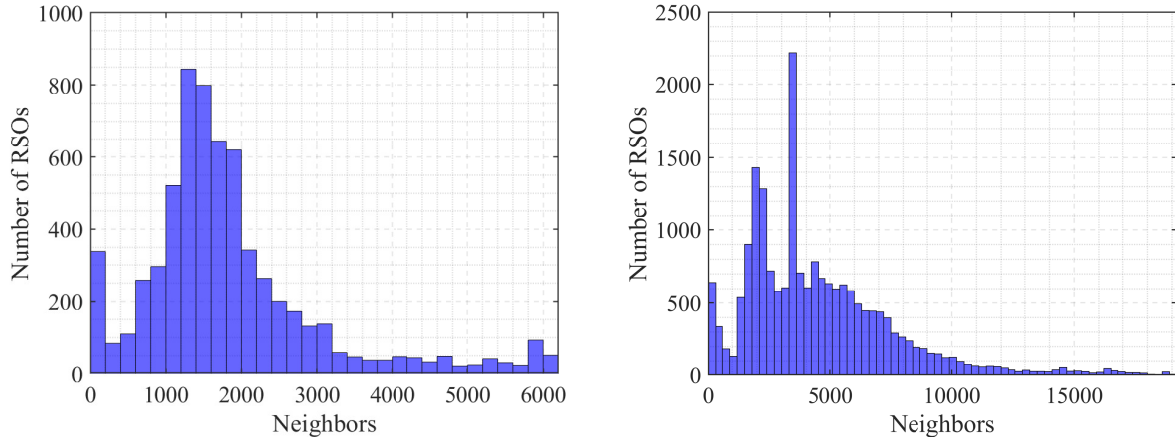


Fig. 16 Neighbors histograms in 2005 (left) and 2022 (right).

Given the impact that the size of the satellites has on the collisions, the objects have been divided according to their size. This data has been obtained from Space Track, where the size is categorized as small, medium, and large. The neighborhoods have been classified according to the size of their main object and Fig. 17 represents the above histograms by distinguishing the neighborhoods according to the size. In both years, the objects with larger neighbor populations are generally of small size, while the smaller neighborhoods usually have a main object of medium or large size. Considering the distribution mode, in 2005 the distribution is more equal between the sizes despite there being a slightly larger number of small objects, however, the number of small objects has grown, by 2022, considerably more than the population of medium and large objects.

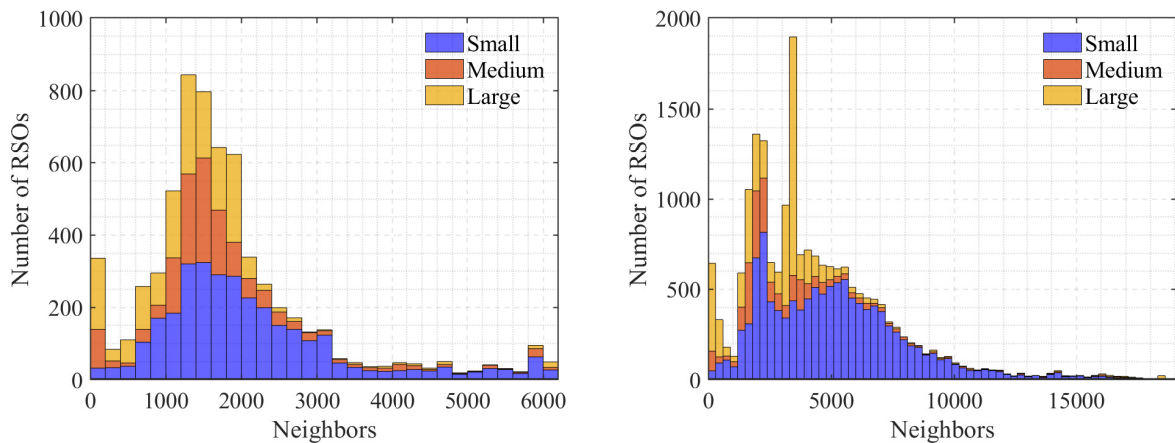


Fig. 17 Neighbors histograms in 2005 (left) and 2022 (right) depending on main object size.

Neighbors Nevertheless, for the study of collisions, the size of both objects involved in the conjunction is of interest, considering a collision of the large-large type to be much more dangerous than a small-small one. Therefore, apart from the study of the neighborhoods, the pairs have been divided into six possible size types depending on the sizes of both objects involved. Figure 18 shows the evolution of the number of pairs that share space occupancy over the years according to this classification.

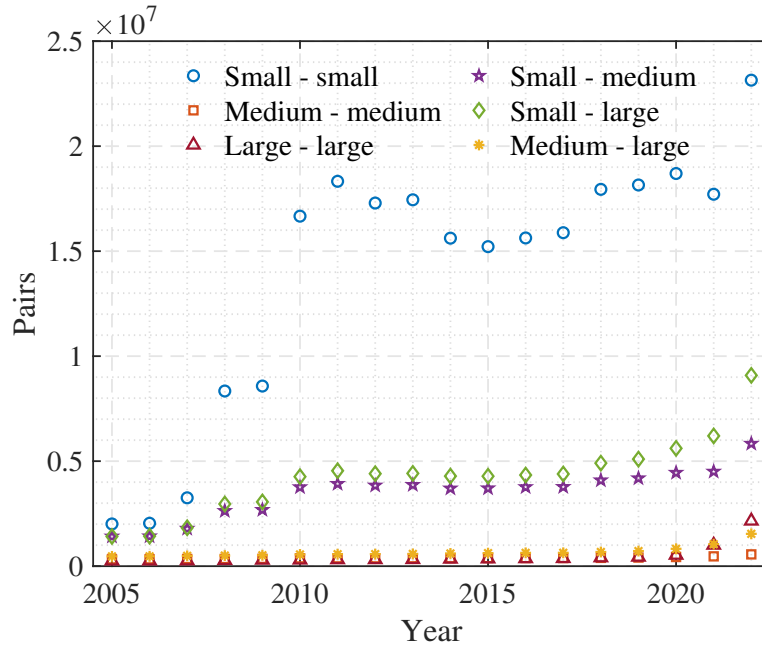


Fig. 18 Evolution of space distribution from 2005 to the present by object size.

Figure 18 shows how pairs involving small objects, in addition to representing the majority of pairs, are the ones that suffer the greatest growth over these years. Otherwise, those pairs concerning only medium or large objects are in the minority and remain fairly constant until the last couple of years when they undergo a slight increase.

Figures 19- 24 show the histograms of the number of neighbors for large and medium RSOs according to their size over the eighteen years analyzed (showing data every five years, and those for the last two years). As the years increase, the neighborhoods become larger. Beginning with the largest number of neighbors at 3000 and ending with a maximum neighborhood of 12000. The largest neighborhoods are those of small objects, those of large to medium-sized objects increased slightly over the years, and most of the RSOs have neighborhoods of large or medium size objects under 1000. It is important to notice the considerable increase in the number of large-large pairs in the last two years. The sudden increase of neighborhoods of 1000-2000 orbits. As is already mentioned, this is mainly due to the launch of the new megaconstellations, whose satellites are generally large in size.

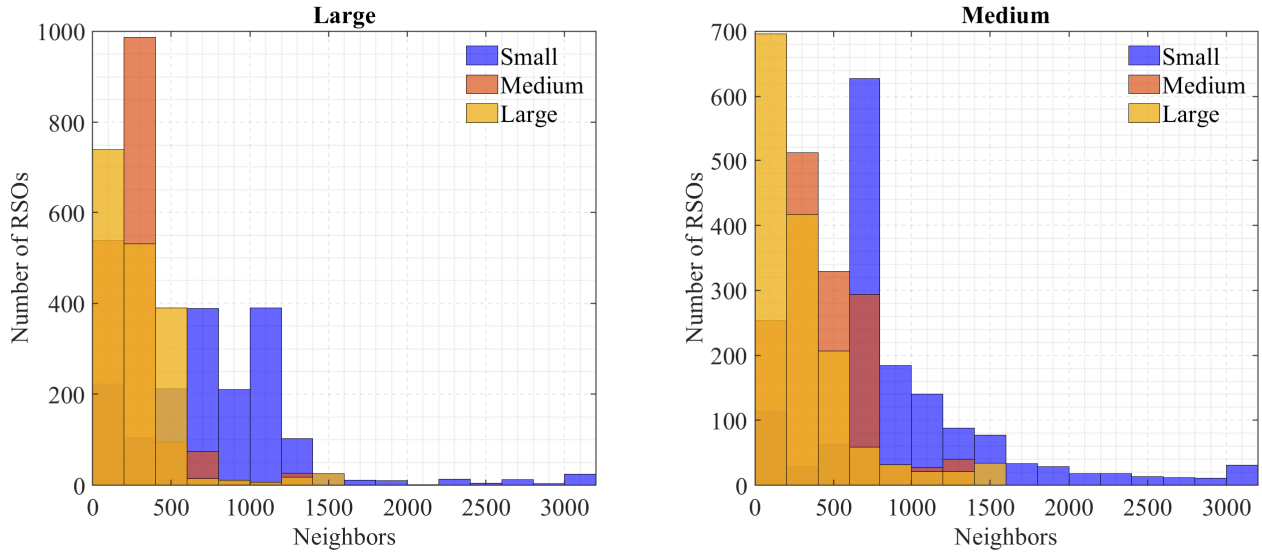


Fig. 19 Neighbors histograms of large (left) and medium (right) main objects in 2005.

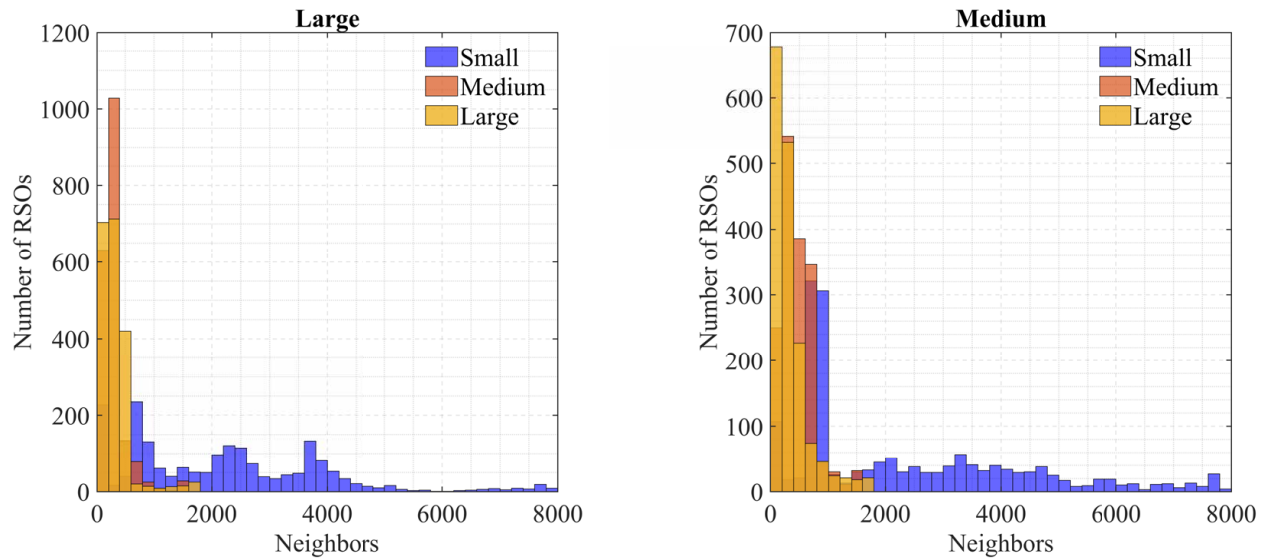


Fig. 20 Neighbors histograms of large (left) and medium (right) main objects in 2010.

V. Conclusion

The concept of short-term space occupancy is a powerful generalization of space occupancy, improving accuracy in those applications with a short time horizon, as is typical in SSA applications.

The use of a series of filters is one of the most widespread computational acceleration techniques for conjunction analyses. The apogee-perigee filter is the simplest of the three classical filters, characterized by its computational simplicity and is typically used as a first stage by more complex filtering algorithms. The newly proposed SO-filter improves the performance of the classical AP-filter taking into account the effect of zonal harmonics, using Cook's model for near-circular orbits, but still maintains a reasonable computational simplicity only requiring the solution of a

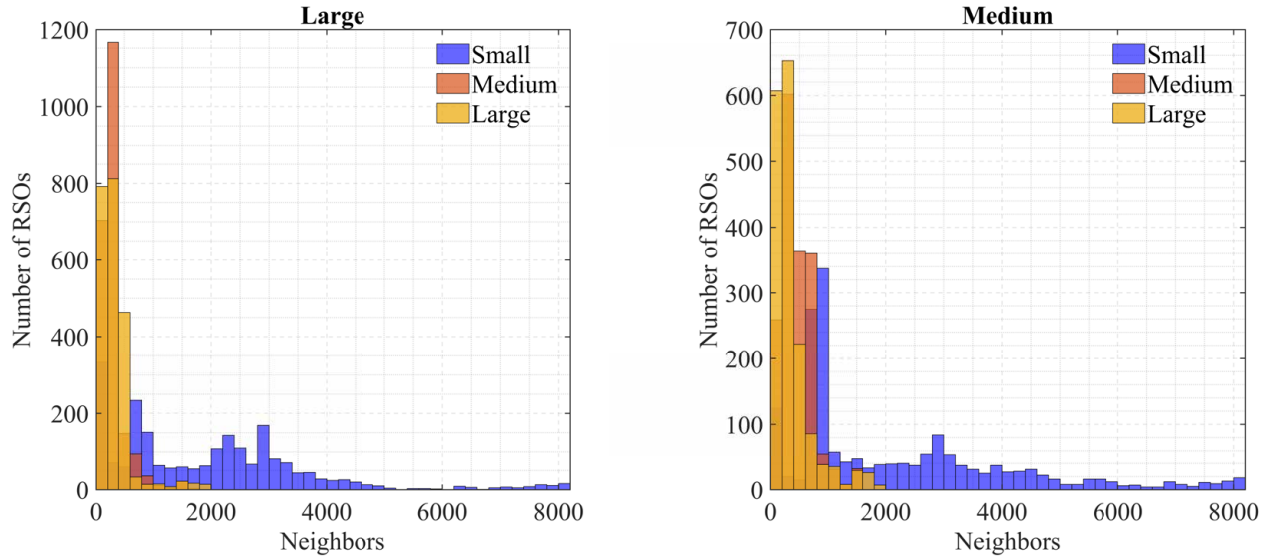


Fig. 21 Neighbors histograms of large (left) and medium (right) main objects in 2015.

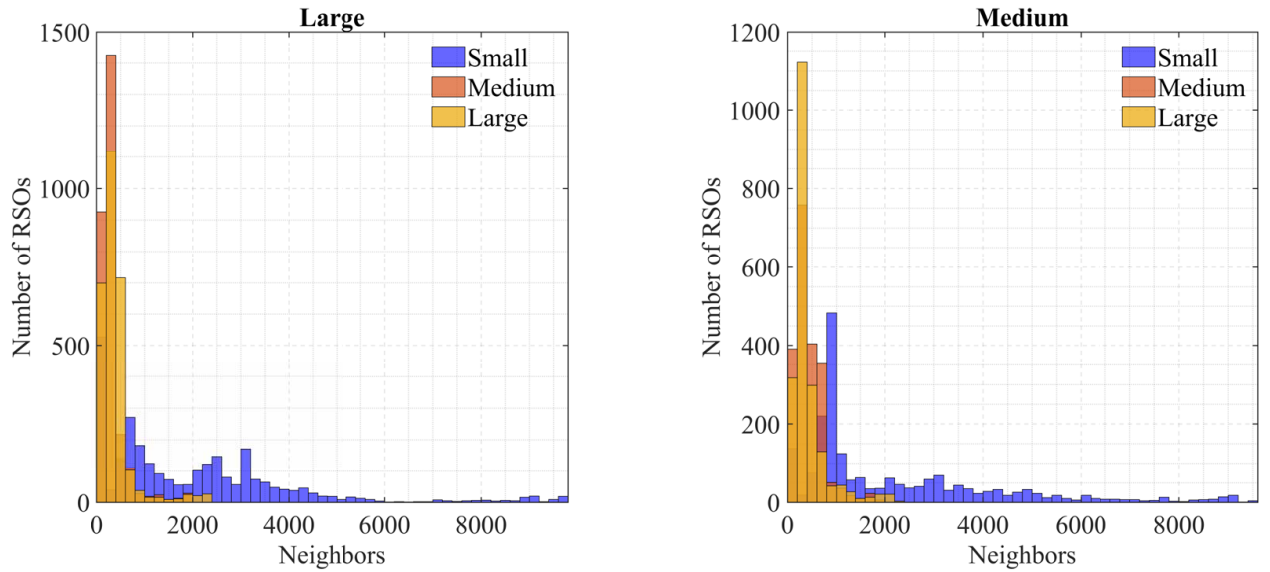


Fig. 22 Neighbors histograms of large (left) and medium (right) main objects in 2020.

quartic.

The performance of the proposed SO-filter has been compared to the performance of the AP-filter and two other versions, a more simplified version (the SOS-filter) and more precise one (the SO-filter exact), by applying them to a large population. The result indicates a considerable improvement in the performance of the SO-filter compared to the classical AP-filter. In addition, SO-filter achieves results comparable to those of the SO-filter exact at a smaller computational cost.

Applying filters without any buffer, the SOS-filter yields twice as many false positives as the AP-filter, but it

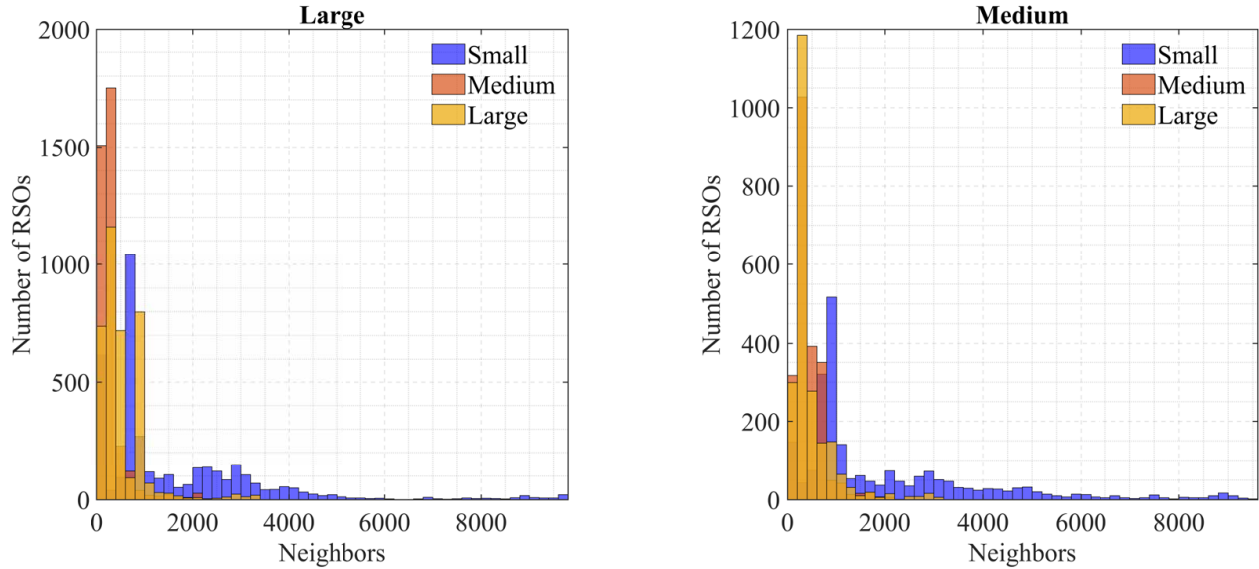


Fig. 23 Neighbors histograms of large (left) and medium (right) main objects in 2021.

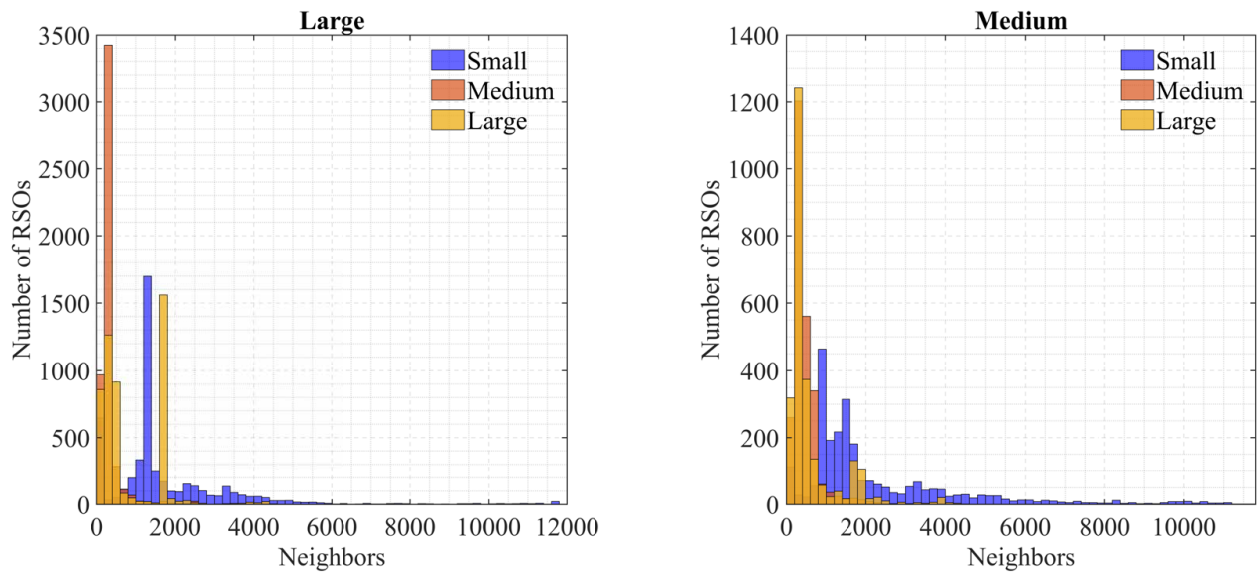


Fig. 24 Neighbors histograms of large (left) and medium (right) main objects in 2022.

reduces false negatives by two order of magnitude. However, the SO-filter reduces false positives by two orders of magnitude, yielding just a 0.007% of false positives, and obtaining eight times fewer false negatives than the AP-filter. Its performance is almost equal to that of the precise filter, with a difference in precision and recall of only 0.001% and 0.005%, respectively. The buffer required for both SO-filter and SOS-filter to remove all false negatives is three times smaller than the one required for the classical filter. Furthermore, 99.5% of the cases require a buffer smaller than 2.2 km with the SOS-filter and 1.25 km with SO-filter, while the AP-filter would require a buffer of 9.81 km to correctly bounds the same percentage. Moreover, setting the buffer according to the categories described, to bound

100% of the orbits, the SOS-filter yields almost three times fewer false positives than the AP-filter, and the SO-filter more than ten times fewer. Among the pairs forwarded by the filter, 15% of them would not require this analysis using the AP-filter, whereas this percentage is reduced to 6% by applying the SOS-filter and to 2% by implementing the SO-filter. In addition, applying a larger buffer at low orbits to account for the effect of atmospheric drag, the comparison between filters is almost equal, decreasing the accuracy by less than 0.05%.

Finally, a brief study of the evolution of the space population over the years shows its significant growth and the improvements in its management, with a decrease in the percentage of couples sharing space occupancy in recent times.

Acknowledgments

The authors acknowledge support by grant TED2021-132099B-C33 funded by MCIN/ AEI/ 10.13039/501100011033 and by “European Union NextGenerationEU/PRTR.” Additional support was provided by MINECO/AEI and FEDER/EU under Project PID2020-112576GB-C21. Ana S. Rivero was funded by a FPU grant from the Spanish Ministry of Universities.

References

- [1] Muelhaupt, T. J., Sorge, M. E., Morin, J., and Wilson, R. S., “Space traffic management in the New Space era,” *Journal of Space Safety Engineering*, Vol. 6, No. 2, 2019, pp. 80–87. <https://doi.org/10.1016/j.jsse.2019.05.007>.
- [2] Adushkin, V., Aksenov, O. Y., Veniaminov, S., Kozlov, S., and Tyurenkova, V., “The small orbital debris population and its impact on space activities and ecological safety,” *Acta Astronautica*, Vol. 176, 2020, pp. 591–597. <https://doi.org/10.1016/j.actaastro.2020.01.015>.
- [3] Sgobba, T., and Allahdadi, F. A., “Orbital Operations Safety,” *Safety Design for Space Operations*, Elsevier, 2013, pp. 411–602. <https://doi.org/10.1016/b978-0-08-096921-3.00008-8>.
- [4] Pardini, C., and Anselmo, L., “Review of past on-orbit collisions among cataloged objects and examination of the catastrophic fragmentation concept,” *Acta astronautica*, Vol. 100, 2014, pp. 30–39. <https://doi.org/10.1016/j.actaastro.2014.03.013>.
- [5] Krage, F. J., *Nasa spacecraft conjunction assessment and collision avoidance best practices handbook*, Technical report, NASA, 2020. URL https://nodis3.gsfc.nasa.gov/OCE_docs/OCE_50.pdf.
- [6] Stevenson, E., Rodriguez-Fernandez, V., Urrutxua, H., and Camacho, D., “Benchmarking deep learning approaches for all-vs-all conjunction screening,” *Advances in Space Research*, 2023. <https://doi.org/10.1016/j.asr.2023.01.036>.
- [7] Escobar, D., Águeda, A., Martín, L., and Martínez, F. M., “Efficient all vs. all collision risk analyses,” *Journal of Aerospace Engineering, Sciences and Applications*, Vol. 4, No. 2, 2012, pp. 40–48. <https://doi.org/10.7446/jaesa.0402.04>.
- [8] Hall, R., Berry, M., Coppola, V., and Woodburn, J., “All-on-all conjunction assessment: Methods for automating and

- minimizing the computation time,” *Advanced Maui Optical and Space Surveillance Technologies Conference*, edited by S. Ryan, 2009, p. E71.
- [9] Healy, L. M., “Close conjunction detection on parallel computer,” *Journal of Guidance, Control, and Dynamics*, Vol. 18, No. 4, 1995, pp. 824–829. <https://doi.org/10.2514/3.21465>.
- [10] Woodburn, J., Coppola, V., and Stoner, F., “A description of filters for minimizing the time required for orbital conjunction computations,” *AAS/AIAA Astrodynamics Specialist Conference*, 2009, pp. 1157–1174.
- [11] Kerr, E., and Sanchez, N., “State of the Art and Future Needs in Conjunction Analysis Methods, Processes and Software,” *Proceedings of 8th European Conference on Space Debris*, 2021, pp. 20–23.
- [12] Hoots, F. R., Crawford, L. L., and Roehrich, R. L., “An analytic method to determine future close approaches between satellites,” *Celestial Mechanics*, Vol. 33, 1984, pp. 143–158. <https://doi.org/10.1007/BF01234152>.
- [13] Algethamie, R., and Armellin, R., “Probability of collision for a newly generated debris cloud using subset simulation technique,” *AIP Conference Proceedings*, Vol. 2226, 2020, p. 050004. <https://doi.org/10.1063/5.0003216>.
- [14] Alfano, S., and Finkleman, D., “On selecting satellite conjunction filter parameters,” *Acta Astronautica*, Vol. 99, 2014, pp. 193–200. <https://doi.org/10.1016/j.actaastro.2014.02.004>.
- [15] Casanova, D., Tardioli, C., and Lemaître, A., “Space debris collision avoidance using a three-filter sequence,” *Monthly Notices of the Royal Astronomical Societ*, Vol. 442, No. 4, 2014, pp. 3235–3242. <https://doi.org/10.1093/mnras/stu1065>.
- [16] Bombardelli, C., Falco, G., Amato, D., and Rosengren, A. J., “Space occupancy in Low-Earth Orbit,” *Journal of Guidance, Control, and Dynamics*, Vol. 44, No. 4, 2021, pp. 684–700. <https://doi.org/10.2514/1.G005371>.
- [17] Cook, G., “Perturbations of near-circular orbits by the Earth’s gravitational potential,” *Planetary and Space Science*, Vol. 14, No. 5, 1966, pp. 433 – 444. [https://doi.org/10.1016/0032-0633\(66\)90015-8](https://doi.org/10.1016/0032-0633(66)90015-8).
- [18] Vallado, D. A., *Fundamentals of astrodynamics and applications*, Vol. 12, Springer Science & Business Media, 2001.
- [19] Kozai, Y., “The motion of a close Earth satellite,” *The Astronomical Journal*, Vol. 64, 1959, pp. 367–377. <https://doi.org/10.1086/107957>.
- [20] Lyddane, R. H., “Small eccentricities or inclinations in the Brouwer theory of the artificial satellite,” *The Astronomical Journal*, Vol. 68, No. 8, 1963, pp. 555–558. <https://doi.org/10.1086/109179>.
- [21] Alarcón-Rodríguez, J., Martínez-Fadrique, F., and Klinkrad, H., “Development of a collision risk assessment tool,” *Advances in Space Research*, Vol. 34, No. 5, 2004, pp. 1120–1124.
- [22] Alarcón Rodríguez, J., Martínez Fadrique, F., and Klinkrad, H., “Collision risk assessment with a “smart sieve” method,” *Joint ESA-NASA Space-Flight Safety Conference*, Vol. 486, 2002, p. 159.

- [23] Rivero, A. S., Bombardelli, C., and Vazquez, R., “Space occupancy conjunction filter,” *AAS/AIAA Space Flight Mechanics Meeting*, 2023.
- [24] Vallado, D. A., Crawford, P., Hujsak, R., and Kelso, T., “Revisiting Spacetrack report# 3: rev 1,” *AIAA/AAS Astrodynamics Specialist Conference and Exhibit*, 2006. <https://doi.org/10.2514/6.2006-6753>.
- [25] Fawcett, T., “An introduction to ROC analysis,” *Pattern Recognition Letters*, Vol. 27, No. 8, 2006, pp. 861–874. <https://doi.org/10.1016/j.patrec.2005.10.010>, ROC Analysis in Pattern Recognition.
- [26] Karrenberg, H. K., “Eclipse fractions for sun-synchronous orbits,” *Ph. D. Thesis*, 1964. URL <https://apps.dtic.mil/sti/citations/AD0603152>.
- [27] Hoots, F. R., and Roehrich, R. L., “Models for propagation of NORAD element sets,” Tech. rep., Aerospace Defense Command Peterson AFB CO Office of Astrodynamics, 1980. <https://doi.org/10.21236/ada093554>.
- [28] Schaub, H., and Junkins, J. L., *Analytical Mechanics of Aerospace Systems*, American Institute of Aeronautics and Astronautics, 2003. <https://doi.org/10.2514/4.861550>.

Appendix: Osculating to mean orbital elements conversions

The algorithm employed to translate the osculating orbit elements into mean orbit elements is outlined in this Appendix. It is based on the theory developed by Kozai [19] and Lyddane [20].

This mapping translates any osculating (instantaneous) orbital elements into mean (orbit averaged, with short period motion removed) orbital element equivalent values. It is important to take into account that only first order J_2 terms are retained in this algorithm, thus small errors of order J_2 are to be expected. As it is explained in Appendix G of Schaub [28], the forward and inverse mapping functions between the mean and osculating orbit elements only differ by a sign, because a first-order truncation is performed for the infinite power series solution. In this Appendix, the equations are written with the signs corresponding to the change from osculating to mean elements (to compute the osculating elements from the mean ones, it is enough to switch the signs of the short-periodic terms).

Let the original osculating orbit elements be given by $(a, e, i, \Omega, \omega, M)$ and the transformed mean orbit elements be given through $(\hat{a}, \hat{e}, \hat{i}, \hat{\Omega}, \hat{\omega}, \hat{M})$. The true anomaly, ν , is computed using Kepler’s equation, given in Eq. (57), and the eccentric anomaly, E , is related with ν through Eq. (58).

$$M = E - e \sin E \tag{57}$$

$$\nu = 2 \tan^{-1} \left(\sqrt{\frac{1+e}{1-e}} \tan \left(\frac{E}{2} \right) \right) \tag{58}$$

Following Kozai, the short-periodic term for the orbital elements of the zonal problem are computed by Eqs. (59)-(64) given next. It is important to notice that the mean values of short-periodic perturbations are not zero, except those of semimajor axis. Therefore, in these equations, their mean values with respect to the mean anomaly are subtracted. This subtraction is the last term of Eqs. (60)-(64).

Semimajor axis:

$$a_{sp} = \frac{J_2}{2a} \left[(2 - 3\kappa) \left(\frac{a^3}{r^3} - \lambda^{-3} \right) + 3\kappa \frac{a^3}{r^3} c_{2,2} \right] \quad (59)$$

Eccentricity:

$$e_{sp} = \frac{\lambda^2}{2e} \frac{3J_2}{a^2} \left[\frac{1}{3} \left(1 - \frac{3}{2}\kappa \right) \left(\frac{a^3}{r^3} - \lambda^{-3} \right) + \frac{1}{2} \frac{a^3}{r^3} \kappa c_{2,2} \right] \\ - \frac{3J_2\kappa}{4ea^2\lambda^2} \left[c_{2,2} + ec_{1,2} + \frac{1}{3}ec_{3,2} \right] - \frac{J_2\kappa e(2\lambda + 1) \cos(2\omega)}{4a^2\lambda^2(\lambda + 1)^2} \quad (60)$$

Inclination:

$$i_{sp} = \frac{J_2}{8a^2\lambda^4} \sin 2i (3c_{2,2} + 3ec_{1,2} + ec_{3,2}) - \frac{J_2 \sin 2i (2\lambda^2 - \lambda - 1) \cos(2\omega)}{8a^2\lambda^4(\lambda + 1)} \quad (61)$$

Argument of pericenter:

$$\omega_{sp} = \frac{3J_2}{2a^2\lambda^4} \left\{ \frac{4 - 5\kappa}{2} (v - M + e s_{1,0}) + \frac{5\kappa - 2}{4} \left(s_{2,2} + e s_{1,2} + \frac{e}{3} s_{3,2} \right) \right. \\ \left. + \frac{1}{e} \left[\left(\frac{2 - 3\kappa}{2} \right) \left[\left(1 - \frac{e^2}{4} \right) s_{1,0} + \frac{e}{2} s_{2,0} + \frac{e^2}{12} s_{3,0} \right] \right. \right. \\ \left. \left. - \kappa \left(\frac{1}{4} \left(1 + \frac{5}{4} e^2 \right) s_{1,2} - \frac{e^2}{16} s_{1,-2} - \frac{7}{12} \left(1 - \frac{e^2}{28} \right) s_{3,2} - \frac{3}{8} e s_{4,2} - \frac{e^2}{16} s_{5,2} \right) \right] \right\} \\ - \frac{3J_2}{2a^2\lambda^4} \left[\frac{\kappa}{8} + \frac{(1 + 2\lambda)(2\kappa\lambda^2 - \lambda^2 - \kappa + 1)}{6(\lambda + 1)^2} \right] \sin(2\omega) \quad (62)$$

Longitude of the ascending node:

$$\Omega_{sp} = -\frac{3J_2}{2a^2\lambda^4} \cos i \left[\nu - M + e \sin \nu - \frac{1}{2}s_{2,2} - \frac{1}{2}es_{1,2} - \frac{1}{6}es_{3,2} \right] - \frac{J_2 \cos i (2\lambda^2 - \lambda - 1) \sin(2\omega)}{4a^2\lambda^4(\lambda + 1)} \quad (63)$$

Mean anomaly:

$$eM_{sp} = \frac{3J_2}{2a^2\lambda^3} \left\{ -\left(1 - \frac{3}{2}\kappa\right) \left[\left(1 - \frac{e^2}{4}\right) \sin \nu + \frac{e}{2} \sin 2\nu + \frac{e^2}{12} \sin 3\nu \right] + \kappa \left[\frac{1}{4} \left(1 + \frac{5}{4}e^2\right) \sin(\nu + 2\omega) - \frac{e^2}{16} \sin(\nu - 2\omega) - \frac{7}{12} \left(1 - \frac{e^2}{28}\right) \sin(3\nu + 2\omega) - \frac{3}{8}e \sin(4\nu + 2\omega) - \frac{e^2}{16} \sin(5\nu + 2\omega) \right] \right\} + \frac{eJ_2\kappa(4\lambda^3 - \lambda^2 - 18\lambda - 9) \sin 2\omega}{16a^2\lambda^3(\lambda + 1)^2} \quad (64)$$

The following terms were used in Eqs. (59)-(64):

$$\lambda = \sqrt{1 - e^2}, \quad \kappa = \sin^2 i, \quad r = \frac{a(1 - e^2)}{1 + e \cos \nu},$$

$$s_{1,0} = \sin \nu, \quad s_{2,0} = \sin 2\nu, \quad s_{3,0} = \sin 3\nu, \quad s_{1,2} = \sin(\nu + 2\omega),$$

$$s_{1,-2} = \sin(\nu - 2\omega), \quad s_{2,2} = \sin(2\nu + 2\omega), \quad s_{3,2} = \sin(3\nu + 2\omega), \quad (65)$$

$$s_{4,2} = \sin(4\nu + 2\omega), \quad s_{5,2} = \sin(5\nu + 2\omega), \quad c_{1,2} = \cos(\nu + 2\omega),$$

$$c_{2,2} = \cos(2\nu + 2\omega), \quad c_{3,2} = \cos(3\nu + 2\omega)$$

These expressions, with the exception of the semimajor axis, are well known to contain singularities both near-circular and/or equatorial orbits. In order to obtain a more robust mapping near these conditions, Lyddane's theory is applied. To provide numerically stable expressions for the mean anomaly and eccentricity short-periodic components, ς and ι are

defined next by Eqs. (67) and (68). Similarly, for the right ascension of the ascending node and the inclination, ρ and ϕ are determined by Eqs. (69) and (69).

$$\zeta = (e - e_{sp}) \cos M + eM_{sp} \sin M \approx (e - e_{sp}) \cos(M - M_{sp}) \quad (66)$$

$$\iota = (e - e_{sp}) \sin M - eM_{sp} \cos M \approx (e - e_{sp}) \sin(M - M_{sp}) \quad (67)$$

$$\rho = \left(\sin \frac{i}{2} - \frac{i_{sp}}{2} \cos \frac{i}{2} \right) \cos \Omega + \sin \frac{i}{2} \sin \Omega \Omega_{sp} \approx \sin \left(\frac{i - i_{sp}}{2} \right) \cos (\Omega - \Omega_{sp}) \quad (68)$$

$$\phi = \left(\sin \frac{i}{2} - \frac{i_{sp}}{2} \cos \frac{i}{2} \right) \sin \Omega + \sin \frac{i}{2} \cos \Omega \Omega_{sp} \approx \sin \left(\frac{i - i_{sp}}{2} \right) \sin (\Omega - \Omega_{sp}) \quad (69)$$

Once these variables are defined, numerically stable expressions for the five orbital elements can be computed with Eqs (71)-(75), whereas the mean semimajor axis is computed by Eq. (70).

$$\hat{a} = a - a_{sp} \quad (70)$$

$$\hat{M} = \tan^{-1} \left(\frac{\iota}{\zeta} \right) \quad (71)$$

$$\hat{e} = \sqrt{\iota^2 + \zeta^2} \quad (72)$$

$$\hat{\Omega} = \tan^{-1} \left(\frac{\phi}{\rho} \right) \quad (73)$$

$$\hat{i} = 2 \sin^{-1} \left(\sqrt{\phi^2 + \rho^2} \right) \quad (74)$$

$$\hat{\omega} = (M - M_{sp}) + (\omega - \omega_{sp}) + (\Omega - \Omega_{sp}) - \hat{M} - \hat{\Omega} \quad (75)$$